

On the robustness and performance of entropy stable discontinuous collocation methods for the compressible Navier–Stokes equations

Diego Rojas^{a,1}, Radouan Boukharfane^{b,2}, Lisandro Dalcin^{b,3}, David C. Del Rey Fernández^{c,d,3}, Hendrik Ranocha^{b,2}, David E. Keyes^{b,4}, Matteo Parsani^{b,5,*}

^a*King Abdullah University of Science and Technology (KAUST), Physical Science and Engineering Division (PSE), Extreme Computing Research Center (ECRC), Thuwal, Saudi Arabia*

^b*King Abdullah University of Science and Technology (KAUST), Computer Electrical and Mathematical Science and Engineering Division (CEMSE), Extreme Computing Research Center (ECRC), Thuwal, Saudi Arabia*

^c*National Institute of Aerospace, Hampton, Virginia, United States*

^d*Computational AeroSciences Branch, NASA Langley Research Center, Hampton, Virginia, United States*

Abstract

In computational fluid dynamics, the demand for increasingly multidisciplinary reliable simulations, for both analysis and design optimization purposes, requires transformational advances in individual components of future solvers. At the algorithmic level, hardware compatibility and efficiency are of paramount importance in determining viability at exascale and beyond. However, equally important (if not more so) is algorithmic robustness with minimal user intervention, which becomes progressively more challenging to achieve as problem size and physics complexity increase. We numerically show that low and high order entropy stable discontinuous spatial discretizations based on summation-by-part operators and simultaneous-approximation-terms technique provide an essential step toward a truly enabling technology in terms of reliability and robustness for both under-resolved turbulent flow simulations and flows with discontinuities.

Keywords: Entropy stability, Discontinuous collocation, Robustness, Summation-by-parts operators, Simultaneous-approximation-terms, Compressible Navier–Stokes equations, Under-resolved turbulence, Non-smooth flows

1. Introduction

Efficient numerical algorithms are sought that exploit $\mathcal{O}(10^9)$ flops 10^9 times per second, or exaflop/s on next-generation data-centric hardware. Hardware compatibility and efficiency are of paramount importance in determining an algorithm’s viability at exascale. Equally important (if not more so) is algorithmic robustness, which becomes progressively more challenging to achieve as problem size and physics complexity increase. The requirement is that every step of the solution chain executes high level of reliability/robustness to minimize user intervention. In computational fluid dynamics (CFD), very compact high-order accurate methods are natural candidates for next-generation hardware because they are accurate, and their ratio of communications to local computations is reduced relative to low order methods of the same accuracy (see, for instance, [Hadri et al.] for sustained petascale production turbulent flow runs).

Among modern, unstructured high order methods we can mention discontinuous collocation (DC), discontinuous Galerkin (DG), spectral difference (SD), and flux reconstruction (FR) methods, which can produce highly accurate solutions with minimum numerical dispersion and dissipation. Although DC, DG, SD, and FR methods are well suited for smooth solutions, numerical instabilities may occur if the flow contains *under-resolved physical features* (e.g., under-resolved turbulent flows) or *discontinuities* (e.g., shocks). A variety of mathematical stabilization strategies are commonly used to alleviate this problem, e.g., filtering [39], artificial dissipation, polynomial de-aliasing through over-integration [32, 50], and weighted essentially non-oscillatory limiters [89], to cite a few. However, such stabilization techniques possess several drawbacks since i) they reduce accuracy [83], ii) they usually

*Corresponding author

Email addresses: `diego.rojasblanco@kaust.edu.sa` (Diego Rojas), `radouan.boukharfane@kaust.edu.sa` (Radouan Boukharfane), `dalcinl@gmail.com` (Lisandro Dalcin), `dcdelrey@gmail.com` (David C. Del Rey Fernández), `hendrik.ranocha@kaust.edu.sa` (Hendrik Ranocha), `david.keyes@kaust.edu.sa` (David E. Keyes), `matteo.parsani@kaust.edu.sa` (Matteo Parsani)

¹Ph.D. student

²Postdoctoral Fellow

³Research Scientist

⁴Professor and ECRC Director

⁵Assistant Professor

require tuning parameters for each problem configuration, and iii) they do not yet possess rigorous stability proofs. Thus, the use of high-order accurate methods for complex flow applications is still problematic, and most commercial and industrial software rely on robust nominally second-order accurate discretizations.

Over the past few years, there have been rapid developments in entropy stable high order methods, which can be proven rigorously to be nonlinearly stable (entropy stable). These discretizations are expected to be an essential component in future CFD solvers for complex practical flow simulations [76]. High order entropy stable schemes are often based on the well known matrix-vector nodal formulation collocated at quadrature points; see, for instance, [39]. Because of the approximation error induced by quadrature, we no longer have the integration by parts property and the chain rule in all cases [64]. However, since integration by parts is an essential ingredient for stability proofs at the continuous level, it is necessary to transfer this property to the discrete level. This is precisely the design goal of summation-by-parts (SBP) methods. SBP operators were developed at first in the context of finite difference schemes [48] and later transferred to other frameworks such as finite volume [54], flux reconstruction [65], and discontinuous Galerkin schemes [5, 31]. The methods used in this article belong to the latter class. In particular, they are based on collocated Legendre–Gauss–Lobatto (LGL) quadrature rules in one space dimension and the corresponding discrete SBP operators on curvilinear, unstructured tensor product elements [5, 56, 59]. The discrete integral and derivative operators associated with this quadrature were shown to satisfy the SBP property (see [20, 80] for a review of SBP operators).

While SBP operators can be viewed as matrix difference operators that are mimetic of integration by parts, additional techniques are necessary to compensate for the lack of the chain rule. For example, ad hoc split form methods have been provided for some PDEs such as Burgers’ equation and the compressible Euler equations [5, 6, 33]. In [5, 25, 59], Carpenter and co-authors demonstrated the generic logic behind the splitting procedure by showing the flux differencing technique with the telescoping property, i.e., a telescoping flux form at the element level (see also [7]). Flux differencing is essentially a high order difference operation on Tadmor’s entropy conservative fluxes [82], and applies to any system

with any given entropy function. Discrete stability over the whole domain is achieved by combining the SBP operator with suitable inter-element coupling procedures and boundary conditions, e.g., the simultaneous-approximation-terms (SATs); see, for instance, Parsani et al. [58, 59], Svård and Özcan [81].

Tadmor’s basic idea has led to the construction of several high order and low order entropy stable schemes (see, for instance, [27, 67]). An alternative approach, developed by Olsson and Olinger [55], Gerritsen and Olsson [36] and Yee et al. [88] (see also [73, 75]), relies on choosing entropy functions that result in a homogeneity property on the compressible Euler fluxes. By using this property, splitting of the compressible Euler fluxes are constructed such that when contracted with the entropy variables result in stability estimates analogous in form to energy estimates obtained for linear PDEs. Thus, discretizing the resulting split form using SBP operators, the nonlinear stability analysis performed at the continuous level is mimicked at the semi-discrete level. However, because of the choice of the entropy functions, these approaches cannot be used for the compressible Navier–Stokes equations.

A complementary and general extension of Tadmor’s ideas to finite domains was initiated by Fisher and co-workers [25, 26] who combined the SBP framework, using classical finite difference SBP operators, with Tadmor’s two-point entropy conservative flux. A key feature of this approach is that it extends directly to the compressible Navier–Stokes equations. The resulting schemes follow the continuous entropy analysis, can be shown to be entropy conservative, and can be made entropy stable by adding appropriate interface dissipation in multi-block domains. This nonlinearly stable approach inherits all of the mechanics of SBP-SAT schemes for the imposition of boundary conditions and inter-element coupling. Therefore, it gives a systematic methodology for discretizing problems on complex geometries [58, 59]. Moreover, by constructing schemes that are discretely mimetic of the continuous stability analysis, the need to assume exact integration in the stability proofs is eliminated (see, for example, the work of Hughes et al. [41]). These ideas have been extended to include discontinuous collocated spectral elements [5, 59], fully- and semi-staggered discontinuous collocated spectral elements [7, 56], Cartesian, semi-staggered, discontinuous collocated spectral elements with p -refinement [7], WENO spectral collocation [87], multidimensional SBP

operators [10, 11], multidimensional staggered SBP operators [19], modal decoupled SBP operators [8], p - and hp -adaptive discontinuous collocated spectral elements [17, 18, 23], and fully discrete entropy stable schemes [29, 66], as well as to a number of PDEs besides the compressible Euler and Navier–Stokes equations (for example, the magneto-hydrodynamics [84] and the shallow water equations [85]).

This paper aims to shed some light on the robustness and cost of high-order accurate entropy stable discontinuous collocation discretizations for compressible viscous flows. The literature that reports robustness studies for standard and entropy stable DC/DG formulations in CFD is scarce and focuses exclusively on inviscid flows [33, 62, 86] or low-speed viscous flows [28, 46]. Hence, a detailed analysis of the numerical simulation of compressible viscous flows with under-resolved physical features or discontinuities is needed, given that the additional dissipation introduced by the viscous terms, despite obvious expectations, may not help in resolving robustness issues.

The paper is organized as follows. In Section 2, we introduce the notation that is extensively used in the article. Section 3 presents the coordinate transformation from physical to computational space and key elements of the general spatial discretization framework in the context of the linear convection-diffusion equation. In Section 4, we briefly introduce the compressible Navier–Stokes equations and give an overview of three algorithms that we use to solve them numerically. These schemes cover entropy stable, split form, and conventional discretization choices. Section 5 presents and discusses the numerical results including accuracy, cost, and robustness of these three discretizations. The test cases used for the study are the propagation of a three-dimensional (3D) isentropic vortex at $\text{Ma}_\infty = 0.5$, a 3D supersonic viscous problem constructed with the method of manufactured solutions at $\text{Re} = 4 \cdot 10^6$ and $\text{Ma} \approx 2.14$, the Taylor–Green vortex at a Reynolds number of $\text{Re} = 1,600$ and $\text{Ma} = 0.05$, a 3D simulation of homogeneous isotropic turbulence at $\text{Re}_\lambda = 192$ and $\text{Ma}_t = 0.62$ with the formation of shocklets, and a 3D supersonic flow past a rod with square cross-section at $\text{Re}_\infty = 10,000$ and $\text{Ma}_\infty = 1.5$. Conclusions are drawn in Section 6.

2. Notation

Partial differential equations (PDEs) are discretized on tensor-product cells having Cartesian computational coordinates denoted by the triple (ξ_1, ξ_2, ξ_3) , where the physical coordinates are denoted by the triple (x_1, x_2, x_3) . Vectors are represented by lowercase bold font, for example \mathbf{u} , while matrices are represented using sans-serif font, for example, \mathbf{B} . Continuous functions on a space-time domain are denoted by capital letters in script font. For example,

$$\mathcal{U}(\xi_1, \xi_2, \xi_3, t) \in L^2([\alpha_1, \beta_1] \times [\alpha_2, \beta_2] \times [\alpha_3, \beta_3] \times [0, T])$$

represents a square integrable function, where t is the temporal coordinate. The restriction of such function onto a set of mesh nodes is denoted by lower case bold font. For example, the restriction of \mathcal{U} onto a grid of $N_1 \times N_2 \times N_3$ nodes is given by the vector

$$\mathbf{u} = [\mathcal{U}(\boldsymbol{\xi}^{(1)}, t), \dots, \mathcal{U}(\boldsymbol{\xi}^{(N)}, t)]^T,$$

where N is the total number of nodes ($N = N_1 N_2 N_3$), and the square brackets are used to delineate vectors and matrices, as well as ranges for variables (the context will make clear which meaning is being used). Moreover, $\boldsymbol{\xi}$ is a vector of vectors constructed from the three vectors $\boldsymbol{\xi}_1$, $\boldsymbol{\xi}_2$, and $\boldsymbol{\xi}_3$, which are vectors of size N_1 , N_2 , and N_3 and contain the coordinates of the mesh in the three computational directions, respectively. Finally, $\boldsymbol{\xi}$ is constructed as

$$\boldsymbol{\xi}(3(i-1) + 1 : 3i) = \boldsymbol{\xi}^{(i)} = [\boldsymbol{\xi}_1(i), \boldsymbol{\xi}_2(i), \boldsymbol{\xi}_3(i)]^T,$$

where the notation $\mathbf{u}(i)$ means the i^{th} entry of the vector \mathbf{u} and $\mathbf{u}(i : j)$ is the subvector constructed from \mathbf{u} using the i^{th} through j^{th} entries (i.e., Matlab notation is used).

Oftentimes, monomials are discussed and the following notation is used:

$$\boldsymbol{\xi}_l^j = [(\boldsymbol{\xi}_l(1))^j, \dots, (\boldsymbol{\xi}_l(N_l))^j]^T,$$

with the convention that $\boldsymbol{\xi}_l^j = \mathbf{0}$ for $j < 0$.

Herein, one-dimensional SBP operators are used to discretize derivatives. The definition of a one-dimensional SBP operator in the ξ_l direction, $l = 1, 2, 3$, is [15, 20, 80]

Definition 1. Summation-by-parts operator for the first derivative: A matrix operator, $\mathbf{D}_{\xi_l}^{(1D)} \in \mathbb{R}^{N_l \times N_l}$, is an SBP operator of degree p approximating the derivative $\frac{\partial}{\partial \xi_l}$ on the domain $\xi_l \in [\alpha_l, \beta_l]$ with nodal distribution $\boldsymbol{\xi}_l$ having N_l nodes, if

1. $\mathbf{D}_{\xi_l}^{(1D)} \boldsymbol{\xi}_l^j = j \boldsymbol{\xi}_l^{j-1}$, $j = 0, 1, \dots, p$;
2. $\mathbf{D}_{\xi_l}^{(1D)} = \left(\mathbf{P}_{\xi_l}^{(1D)} \right)^{-1} \mathbf{Q}_{\xi_l}^{(1D)}$, where the norm matrix, $\mathbf{P}_{\xi_l}^{(1D)}$, is symmetric positive definite;
3. $\mathbf{Q}_{\xi_l}^{(1D)} = \left(\mathbf{S}_{\xi_l}^{(1D)} + \frac{1}{2} \mathbf{E}_{\xi_l}^{(1D)} \right)$, $\mathbf{S}_{\xi_l}^{(1D)} = - \left(\mathbf{S}_{\xi_l}^{(1D)} \right)^T$, $\mathbf{E}_{\xi_l}^{(1D)} = \left(\mathbf{E}_{\xi_l}^{(1D)} \right)^T$,
 $\mathbf{E}_{\xi_l}^{(1D)} = \text{diag}(-1, 0, \dots, 0, 1) = \mathbf{e}_N \mathbf{e}_N^T - \mathbf{e}_1 \mathbf{e}_1^T$, $\mathbf{e}_1 = [1, 0, \dots, 0]^T$, and $\mathbf{e}_N = [0, 0, \dots, 1]^T$.

Thus, a degree p SBP operator is one that differentiates exactly monomials up to degree p .

In this work, one-dimensional SBP operators are extended to multiple dimensions using tensor products (\otimes). The tensor product between the matrices \mathbf{A} and \mathbf{B} is given as $\mathbf{A} \otimes \mathbf{B}$. When referencing individual entries in a matrix the notation $\mathbf{A}(i, j)$ is used, which means the i^{th} j^{th} entry in the matrix \mathbf{A} .

The focus of this paper is exclusively on diagonal-norm SBP operators. Moreover, the same one-dimensional SBP operator is used in each direction, each operating on N_l nodes. Specifically, diagonal-norm SBP operators constructed on the Legendre–Gauss–Lobatto (LGL) nodes are used, i.e., a discontinuous collocated spectral element approach is utilized (see, for instance, [5, 33, 35, 56, 59]).

When solving PDEs numerically, the physical domain $\Omega \subset \mathbb{R}^3$, with boundary $\Gamma = \partial\Omega$, with Cartesian coordinates $(x_1, x_2, x_3) \in \mathbb{R}^3$, is partitioned into K non-overlapping elements. The domain of the κ^{th} element is denoted by Ω_κ and has boundary $\partial\Omega_\kappa$. Numerically, we solve PDEs in computational coordinates, $(\xi_1, \xi_2, \xi_3) \in \mathbb{R}^3$, where each Ω_κ is locally transformed to the reference element $\widehat{\Omega}_\kappa$, with boundary $\partial\widehat{\Omega}_\kappa$, using a pull-back curvilinear coordinate transformation which satisfies the following assumption:

Assumption 1. *Each element in physical space is transformed using a local and invertible curvilinear coordinate transformation that is compatible at shared interfaces, meaning that the push-forward element-wise mappings are continuous across physical element interfaces. Note that this is the standard assumption requiring that the curvilinear coordinate transformation is water-tight.*

Precisely, one maps from the reference coordinates $(\xi_1, \xi_2, \xi_3) \in [-1, 1]^3$ to the physical element by the push-forward transformation

$$(x_1, x_2, x_3) = X(\xi_1, \xi_2, \xi_3), \quad (1)$$

which, in the presence of curved elements, is usually a high-order degree polynomial.

3. The linear convection-diffusion equation

Many of the technical details for constructing conservative and stable discretizations for the compressible Navier–Stokes can be presented in the simple context of the linear convection-diffusion equation. The linear convection-diffusion equation in Cartesian physical coordinates is given as

$$\begin{aligned} \frac{\partial \mathcal{U}}{\partial t} + \sum_{m=1}^3 \frac{\partial (a_m \mathcal{U})}{\partial x_m} &= \sum_{m=1}^3 \frac{\partial^2 (b_m \mathcal{U})}{\partial x_m^2}, \quad \forall (x_1, x_2, x_3) \in \Omega, \quad t \geq 0, \\ \mathcal{U}(x_1, x_2, x_3, t) &= \mathcal{G}^{(B)}(x_1, x_2, x_3, t), \quad \forall (x_1, x_2, x_3) \in \Gamma, \quad t \geq 0, \\ \mathcal{U}(x_1, x_2, x_3, 0) &= \mathcal{G}^{(0)}(x_1, x_2, x_3), \quad \forall (x_1, x_2, x_3) \in \Omega, \end{aligned} \quad (2)$$

where $(a_m \mathcal{U})$ are the inviscid fluxes, a_m are the (constant) components of the convection speed, $\frac{\partial (b_m \mathcal{U})}{\partial x_m}$ are the viscous fluxes, and b_m are the (constant and positive) diffusion coefficients. The boundary data, $\mathcal{G}^{(B)}$, and the initial condition, $\mathcal{G}^{(0)}$, are assumed to be in $L^2(\Omega)$, with the further assumption that $\mathcal{G}^{(B)}$ is prescribed so that either energy conservation or energy stability is achieved.

Since derivatives are approximated with differentiation operators defined in computational space, we use the Jacobian of the push-forward mapping and the chain rule

$$\frac{\partial}{\partial x_m} = \sum_{l=1}^3 \frac{\partial \xi_l}{\partial x_m} \frac{\partial}{\partial \xi_l}, \quad \frac{\partial^2}{\partial x_m^2} = \sum_{l,a=1}^3 \frac{\partial \xi_l}{\partial x_m} \frac{\partial}{\partial \xi_l} \left(\frac{\partial \xi_a}{\partial x_m} \frac{\partial}{\partial \xi_a} \right),$$

to transform eq. (2) from physical to computational space as

$$\mathcal{J} \frac{\partial \mathcal{U}}{\partial t} + \sum_{l,m=1}^3 \mathcal{J} \frac{\partial \xi_l}{\partial x_m} \frac{\partial (a_m \mathcal{U})}{\partial \xi_l} = \sum_{l,a,m=1}^3 \mathcal{J} \frac{\partial \xi_l}{\partial x_m} \frac{\partial}{\partial \xi_l} \left(\frac{\partial \xi_a}{\partial x_m} \frac{\partial (b_m \mathcal{U})}{\partial \xi_a} \right), \quad (3)$$

where \mathcal{J} is the determinant of the metric Jacobian. Bringing the metric terms $\mathcal{J} \frac{\partial \xi_l}{\partial x_m}$ inside the derivative, and using the product rule, gives

$$\begin{aligned} \mathcal{J} \frac{\partial \mathcal{U}}{\partial t} + \sum_{l,m=1}^3 \frac{\partial}{\partial \xi_l} \left(\mathcal{J} \frac{\partial \xi_l}{\partial x_m} a_m \mathcal{U} \right) - \sum_{l,m=1}^3 a_m \mathcal{U} \frac{\partial}{\partial \xi_l} \left(\mathcal{J} \frac{\partial \xi_l}{\partial x_m} \right) = \\ \sum_{l,a,m=1}^3 \frac{\partial}{\partial \xi_l} \left(\mathcal{J} \frac{\partial \xi_l}{\partial x_m} \frac{\partial \xi_a}{\partial x_m} \frac{\partial (b_m \mathcal{U})}{\partial \xi_a} \right) - \sum_{l,a,m=1}^3 \frac{\partial \xi_a}{\partial x_m} \frac{\partial (b_m \mathcal{U})}{\partial \xi_a} \frac{\partial}{\partial \xi_l} \left(\mathcal{J} \frac{\partial \xi_l}{\partial x_m} \right). \end{aligned} \quad (4)$$

The last terms on the left- and right-hand sides of eq. (4) are zero via the GCL relations

$$\sum_{l=1}^3 \frac{\partial}{\partial \xi_l} \left(\mathcal{J} \frac{\partial \xi_l}{\partial x_m} \right) = 0, \quad m = 1, 2, 3, \quad (5)$$

leading to the strong conservation form of the convection-diffusion equation in computational space

$$\mathcal{J} \frac{\partial \mathcal{U}}{\partial t} + \sum_{l,m=1}^3 \frac{\partial}{\partial \xi_l} \left(\mathcal{J} \frac{\partial \xi_l}{\partial x_m} a_m \mathcal{U} \right) = \sum_{l,a,m=1}^3 \frac{\partial}{\partial \xi_l} \left(\mathcal{J} \frac{\partial \xi_l}{\partial x_m} \frac{\partial \xi_a}{\partial x_m} \frac{\partial (b_m \mathcal{U})}{\partial \xi_a} \right). \quad (6)$$

Now, consider discretizing eq. (6) by using the following differentiation matrices

$$\mathbf{D}_{\xi_1} = \mathbf{D}_{\xi_1}^{(1D)} \otimes \mathbf{I}_{N_2} \otimes \mathbf{I}_{N_3}, \quad \mathbf{D}_{\xi_2} = \mathbf{I}_{N_1} \otimes \mathbf{D}_{\xi_2}^{(1D)} \otimes \mathbf{I}_{N_3}, \quad \mathbf{D}_{\xi_3} = \mathbf{I}_{N_1} \otimes \mathbf{I}_{N_2} \otimes \mathbf{D}_{\xi_3}^{(1D)},$$

where \mathbf{I}_{N_l} is an $N_l \times N_l$ identity matrix and N_l is the number of LGL points per direction in a given element. The diagonal matrix containing the metric Jacobian is defined as

$$\mathbf{J}_\kappa = \text{diag} \left(\mathcal{J}(\boldsymbol{\xi}^{(1)}), \dots, \mathcal{J}(\boldsymbol{\xi}^{(N_\kappa)}) \right),$$

while the diagonal matrix of the metric terms, $\left[\mathcal{J} \frac{\partial \xi_l}{\partial x_m} \right]_\kappa$, has to be chosen to be a discretization of

$$\text{diag} \left(\mathcal{J} \frac{\partial \xi_l}{\partial x_m}(\boldsymbol{\xi}^{(1)}), \dots, \mathcal{J} \frac{\partial \xi_l}{\partial x_m}(\boldsymbol{\xi}^{(N_\kappa)}) \right),$$

where $N_\kappa = N_1 N_2 N_3$ is the total number of nodes in element κ . Using this nomenclature, the discretization of eq. (6) on the κ^{th} element reads

$$\mathbf{J}_\kappa \frac{d\mathbf{u}_\kappa}{dt} + \sum_{l,m=1}^3 a_m \mathbf{D}_{\xi_l} \left[\mathcal{J} \frac{\partial \xi_l}{\partial x_m} \right]_\kappa \mathbf{u}_\kappa = \sum_{l,m,a=1}^3 b_m \mathbf{D}_{\xi_l} \mathbf{J}_\kappa^{-1} \left[\mathcal{J} \frac{\partial \xi_l}{\partial x_m} \right]_\kappa \left[\mathcal{J} \frac{\partial \xi_a}{\partial x_m} \right]_\kappa \mathbf{D}_{\xi_a} \mathbf{u}_\kappa + \mathbf{SAT}_\kappa, \quad (7)$$

where \mathbf{SAT}_κ is the vectors of the SATs used to impose boundary conditions and inter-element connectivity [6, 58]. The \mathbf{SAT}_κ vector is in general composed from inviscid and viscous contributions, i.e. $\mathbf{SAT}_\kappa = \mathbf{SAT}_\kappa^{(I)} + \mathbf{SAT}_\kappa^{(V)}$.

Unfortunately, the scheme (7) is not guaranteed to be stable. However, a well-known remedy is to canonically split the inviscid terms into one half of the inviscid terms in (3) and one half of the inviscid terms in (4) (see, for instance, [6]), while the viscous terms are treated in strong conservation form. In the continuum, this process leads to

$$\begin{aligned} & \mathcal{J} \frac{\partial \mathcal{U}}{\partial t} + \frac{1}{2} \sum_{l,m=1}^3 \left\{ \frac{\partial}{\partial \xi_l} \left(\mathcal{J} \frac{\partial \xi_l}{\partial x_m} a_m \mathcal{U} \right) + \mathcal{J} \frac{\partial \xi_l}{\partial x_m} \frac{\partial}{\partial \xi_l} (a_m \mathcal{U}) \right\} \\ & - \frac{1}{2} \sum_{l,m=1}^3 \left\{ a_m \mathcal{U} \frac{\partial}{\partial \xi_l} \left(\mathcal{J} \frac{\partial \xi_l}{\partial x_m} \right) \right\} = \sum_{l,a,m=1}^3 \frac{\partial}{\partial \xi_l} \left(\mathcal{J} \frac{\partial \xi_l}{\partial x_m} \frac{\partial \xi_a}{\partial x_m} \frac{\partial (b_m \mathcal{U})}{\partial \xi_a} \right), \end{aligned} \quad (8)$$

where the last set of terms on the left-hand side are zero by the GCL conditions (5). Then, a stable semi-discrete form is constructed in the same manner as the split form (8) by discretizing the inviscid portion of (3) and (6) using \mathbf{D}_{ξ_l} , \mathbf{J}_κ , and $\left[\mathcal{J} \frac{\partial \xi_l}{\partial x_m} \right]_\kappa$, and by averaging the results. The viscous terms result from the discretization of the viscous portion of eq. (6).

This procedure yields

$$\begin{aligned} & \mathbf{J}_\kappa \frac{d\mathbf{u}_\kappa}{dt} + \frac{1}{2} \sum_{l,m=1}^3 a_m \left\{ \mathbf{D}_{\xi_l} \left[\mathcal{J} \frac{\partial \xi_l}{\partial x_m} \right]_\kappa + \left[\mathcal{J} \frac{\partial \xi_l}{\partial x_m} \right]_\kappa \mathbf{D}_{\xi_l} \right\} \mathbf{u}_\kappa \\ & - \frac{1}{2} \sum_{l,m=1}^3 \left\{ a_m \text{diag}(\mathbf{u}_\kappa) \mathbf{D}_{\xi_l} \left[\mathcal{J} \frac{\partial \xi_l}{\partial x_m} \right]_\kappa \mathbf{1}_\kappa \right\} = \\ & \sum_{l,m,a=1}^3 b_m \mathbf{D}_{\xi_l} \mathbf{J}_\kappa^{-1} \left[\mathcal{J} \frac{\partial \xi_l}{\partial x_m} \right]_\kappa \left[\mathcal{J} \frac{\partial \xi_a}{\partial x_m} \right]_\kappa \mathbf{D}_{\xi_a} \mathbf{u}_\kappa + \mathbf{SAT}_\kappa, \end{aligned} \quad (9)$$

where $\mathbf{1}_\kappa$ is a vector of ones of size N_κ .

As in the continuous case, the semi-discrete form has a set of discrete GCL conditions

$$\sum_{l=1}^3 \mathbf{D}_{\xi_l} \left[\mathcal{J} \frac{\partial \xi_l}{\partial x_m} \right]_\kappa \mathbf{1}_\kappa = \mathbf{0}, \quad m = 1, 2, 3, \quad (10)$$

that, when satisfied, lead to the following telescoping, provably stable, semi-discrete form

$$\begin{aligned} \mathbf{J}_\kappa \frac{d\mathbf{u}_\kappa}{dt} + \frac{1}{2} \sum_{l,m=1}^3 a_m \left\{ \mathbf{D}_{\xi_l} \left[\mathcal{J} \frac{\partial \xi_l}{\partial x_m} \right]_\kappa + \left[\mathcal{J} \frac{\partial \xi_l}{\partial x_m} \right]_\kappa \mathbf{D}_{\xi_l} \right\} \mathbf{u}_\kappa = \\ \sum_{l,m,a=1}^3 b_m \mathbf{D}_{\xi_l} \mathbf{J}_\kappa^{-1} \left[\mathcal{J} \frac{\partial \xi_l}{\partial x_m} \right]_\kappa \left[\mathcal{J} \frac{\partial \xi_a}{\partial x_m} \right]_\kappa \mathbf{D}_{\xi_a} \mathbf{u}_\kappa + \mathbf{SAT}_\kappa. \end{aligned} \quad (11)$$

Herein, we consider only conforming interfaces and optimize the metric terms, $\left[\mathcal{J} \frac{\partial \xi_l}{\partial x_m} \right]_\kappa$, as presented in [53]:

- The surface metric terms are specified using analytic metrics,
- Each discrete GCL system (10) is highly underdetermined and is solved using an optimization approach that minimizes the difference between the numerical and analytic volume metrics.

In contrast to the metrics for the inviscid terms, the metrics used for the viscous terms need only be, at worst, consistent and design order approximations. Herein, we use the analytic metrics for the viscous terms calculation.

To make the presentation easier and to introduce the general discretization that will later be used for the viscous portion of the compressible Navier–Stokes equations, the inviscid term is lumped into $\mathcal{I}^{(1)}$, while the viscous terms are simplified. Thus, eq. (8) reduces to

$$\begin{aligned} \mathcal{J} \frac{\partial \mathcal{U}}{\partial t} + \mathcal{I}^{(1)} = \sum_{l,a=1}^3 \frac{\partial}{\partial \xi_l} \left(\widehat{\mathcal{C}}_{l,a} \Theta_a \right), \\ \widehat{\mathcal{C}}_{l,a} = \sum_{m=1}^3 \mathcal{J} \frac{\partial \xi_l}{\partial x_m} \frac{\partial \xi_a}{\partial x_m} b_m, \quad \Theta_a = \frac{\partial \mathcal{U}}{\partial \xi_a}. \end{aligned} \quad (12)$$

A local discontinuous Galerkin (LDG) and interior penalty approach (IP) approach are used (see references [6, 56, 58]). In the LDG approach, the discretization of the viscous terms in eq. (12) proceeds in two steps. First, the gradients Θ_a are discretized, then the derivatives of the viscous fluxes are discretized. Notice that all the metric terms are contained in $\widehat{\mathcal{C}}_{l,a}$, and therefore the critical requirement for stability is to use an SBP operator [6, 22, 58].

Plugging everything together, the final discretization reads

$$\mathbf{J}_\kappa \frac{d\mathbf{u}_\kappa}{dt} + \mathbf{I}_\kappa^{(I)} = \sum_{l,a=1}^3 \mathbf{D}_{\xi_l} \left[\widehat{\mathcal{C}}_{l,a} \right]_\kappa \boldsymbol{\theta}_a^\kappa + \mathbf{SAT}_\kappa^{(I)} + \mathbf{SAT}_\kappa^{(V)}, \quad \boldsymbol{\theta}_a^\kappa = \mathbf{D}_{\xi_a} \mathbf{u}_\kappa + \mathbf{SAT}_\kappa^\theta, \quad (13)$$

where the inviscid contributions are contained in $\mathbf{I}_\kappa^{(I)}$, while $\mathbf{SAT}_\kappa^\theta$ contains the LDG penalty on the gradient of the variables [58]. The proposed discretization of the viscous terms telescopes the viscous fluxes to the boundary and adds a dissipative term [58]. Thus, it mimics the continuous energy analysis, and leads to a provably energy stable discretization, provided appropriate boundary SATs are used.

4. Discretization of the compressible Navier–Stokes equations

In this section, the algorithm for the convection-diffusion equation presented in the previous section is applied to the compressible Navier–Stokes. These equations in Cartesian coordinates read

$$\begin{aligned} \frac{\partial \mathcal{Q}}{\partial t} + \sum_{m=1}^3 \frac{\partial \mathcal{F}_{x_m}^{(I)}}{\partial x_m} &= \sum_{m=1}^3 \frac{\partial \mathcal{F}_{x_m}^{(V)}}{\partial x_m}, & \forall (x_1, x_2, x_3) \in \Omega, \quad t \geq 0, \\ \mathcal{Q}(x_1, x_2, x_3, t) &= \mathcal{G}^{(B)}(x_1, x_2, x_3, t), & \forall (x_1, x_2, x_3) \in \Gamma, \quad t \geq 0, \\ \mathcal{Q}(x_1, x_2, x_3, 0) &= \mathcal{G}^{(0)}(x_1, x_2, x_3), & \forall (x_1, x_2, x_3) \in \Omega, \end{aligned} \quad (14)$$

where the vectors \mathcal{Q} , $\mathcal{F}_{x_m}^{(I)}$ and $\mathcal{F}_{x_m}^{(V)}$ denote the conserved variables, the inviscid fluxes, and the viscous fluxes, respectively. The boundary data, $\mathcal{G}^{(B)}$, and the initial condition, $\mathcal{G}^{(0)}$, are assumed to be in $L^2(\Omega)$, with the further assumption that $\mathcal{G}^{(B)}$ will be set to coincide with linear, well-posed boundary conditions, prescribed in such a way that either entropy conservation or entropy stability is achieved.

The vector of conserved variables is given by

$$\mathcal{Q} = [\rho, \rho \mathcal{U}_1, \rho \mathcal{U}_2, \rho \mathcal{U}_3, \rho \mathcal{E}]^\top,$$

where ρ denotes the density, $\mathbf{u} = [\mathcal{U}_1, \mathcal{U}_2, \mathcal{U}_3]^\top$ is the velocity vector, and \mathcal{E} is the specific total energy. The inviscid fluxes are given as

$$\mathcal{F}_{x_m}^{(I)} = [\rho \mathcal{U}_m, \rho \mathcal{U}_m \mathcal{U}_1 + \delta_{m,1} \mathcal{P}, \rho \mathcal{U}_m \mathcal{U}_2 + \delta_{m,2} \mathcal{P}, \rho \mathcal{U}_m \mathcal{U}_3 + \delta_{m,3} \mathcal{P}, \rho \mathcal{U}_m \mathcal{H}]^\top, \quad (15)$$

where \mathcal{P} is the pressure, \mathcal{H} is the specific total enthalpy and $\delta_{i,j}$ is the Kronecker delta.

The required constituent relations are

$$\mathcal{H} = c_p \mathcal{T} + \frac{1}{2} \mathbf{u}^T \mathbf{u}, \quad \mathcal{P} = \rho R \mathcal{T}, \quad R = \frac{R_u}{M_w},$$

where \mathcal{T} is the temperature, R_u is the universal gas constant, M_w is the molecular weight of the gas, and c_p is the specific heat capacity at constant pressure. Finally, the specific thermodynamic entropy is given as

$$s = \frac{R}{\gamma - 1} \log \left(\frac{\mathcal{T}}{\mathcal{T}_\infty} \right) - R \log \left(\frac{\rho}{\rho_\infty} \right), \quad \gamma = \frac{c_p}{c_p - R},$$

where \mathcal{T}_∞ and ρ_∞ are the reference temperature and density, respectively (the stipulated convention has been broken here and s has been used rather than \mathcal{S} for reasons that will be clear next).

The viscous fluxes $\mathcal{F}_{x_m}^{(V)}$ are given by

$$\mathcal{F}_{x_m}^{(V)} = \left[0, \tau_{1,m}, \tau_{2,m}, \tau_{3,m}, \sum_{i=1}^3 \tau_{i,m} \mathcal{U}_i - \kappa \frac{\partial \mathcal{T}}{\partial x_m} \right]^T, \quad (16)$$

while the viscous stresses are defined as

$$\tau_{i,j} = \mu \left(\frac{\partial \mathcal{U}_i}{\partial x_j} + \frac{\partial \mathcal{U}_j}{\partial x_i} - \delta_{i,j} \frac{2}{3} \sum_{n=1}^3 \frac{\partial \mathcal{U}_n}{\partial x_n} \right), \quad (17)$$

where $\mu(\mathcal{T})$ is the dynamic viscosity and $\kappa(\mathcal{T})$ is the thermal conductivity.

The compressible Navier–Stokes equations given in eq. (19) have a convex extension, that when integrated over the physical domain, Ω , depends only on the boundary data and negative semi-definite dissipation terms. This convex extension depends on an entropy function, \mathcal{S} , that is constructed from the thermodynamic entropy as

$$\mathcal{S} = -\rho s,$$

and provides a mechanism for proving stability in the L^2 norm. The entropy variables \mathcal{W} are an alternative variable set related to the conservative variables via a one-to-one mapping. They are defined in terms of the entropy function \mathcal{S} by the relation $\mathcal{W}^T = \partial \mathcal{S} / \partial \mathcal{Q}$ and they

are extensively used in the entropy stability proofs of the algorithms used herein; see for instance [5, 18, 30, 56]. In addition, they simultaneously symmetrize the inviscid and the viscous flux Jacobians in all three spatial directions. Further details on continuous entropy analysis are available elsewhere [6, 12, 59].

The entropy stability for the viscous terms in the compressible Navier–Stokes equations (19) is readily demonstrated by exploiting the symmetrizing properties of the entropy variables. Thus, we recast the viscous fluxes in terms of the entropy variables

$$\mathcal{F}_{x_m}^{(V)} = \sum_{j=1}^3 \mathbf{C}_{m,j} \frac{\partial \mathcal{W}}{\partial x_j}, \quad (18)$$

with the flux Jacobian matrices satisfying $\mathbf{C}_{m,j} = (\mathbf{C}_{j,m})^\top$.

Furthermore, in order to apply the algorithm outlined for the convection-diffusion case to the compressible Navier–Stokes equations, we have to recast system (14) in a skew-symmetric form with respect to the metric terms. This procedure results in

$$\mathcal{J} \frac{\partial \mathcal{Q}}{\partial t} + \sum_{l,m=1}^3 \frac{1}{2} \frac{\partial}{\partial \xi_l} \left(\mathcal{J} \frac{\partial \xi_l}{\partial x_m} \mathcal{F}_{x_m}^{(I)} \right) + \frac{1}{2} \mathcal{J} \frac{\partial \xi_l}{\partial x_m} \frac{\partial \mathcal{F}_{x_m}^{(I)}}{\partial \xi_l} = \sum_{l,m=1}^3 \frac{\partial}{\partial \xi_l} \left(\mathcal{J} \frac{\partial \xi_l}{\partial x_m} \mathcal{F}_{x_m}^{(V)} \right), \quad (19)$$

where the GCL relations given in eq. (5) are used to obtain eq. (20) from the divergence form (14). Substituting eq. (18) into eq. (19), we arrive at the system of equations

$$\mathcal{J} \frac{\partial \mathcal{Q}}{\partial t} + \sum_{l,m=1}^3 \frac{1}{2} \frac{\partial}{\partial \xi_l} \left(\mathcal{J} \frac{\partial \xi_l}{\partial x_m} \mathcal{F}_{x_l} \right) + \frac{1}{2} \mathcal{J} \frac{\partial \xi_l}{\partial x_m} \frac{\partial \mathcal{F}_{x_m}}{\partial \xi_l} = \sum_{l,a=1}^3 \frac{\partial}{\partial \xi_l} \left(\hat{\mathbf{C}}_{l,a} \frac{\partial \mathcal{W}}{\partial \xi_a} \right), \quad (20)$$

where

$$\hat{\mathbf{C}}_{l,a} = \mathcal{J} \frac{\partial \xi_l}{\partial x_m} \sum_{m,j=1}^3 \mathbf{C}_{m,j} \frac{\partial \xi_a}{\partial x_j}. \quad (21)$$

The symmetric properties of the viscous flux Jacobians are preserved by the rotation into curvilinear coordinates, i.e. $\hat{\mathbf{C}}_{l,a} = (\hat{\mathbf{C}}_{a,l})^\top$. We remark that this form of the equations, i.e. skew-symmetric form plus the quadratic form of the viscous terms, is necessary for the construction of the entropy stable schemes used in this work. For further details on the derivation of these viscous coefficient matrices see [24, 59].

The discretization of the compressible Euler equations, i.e., the inviscid part of (20), is given by

$$\mathbf{J}_\kappa \frac{d\mathbf{q}_\kappa}{dt} + \frac{1}{2} \sum_{l,m=1}^3 \left(\mathbf{D}_{\xi_l} \left[\mathcal{J} \frac{\partial \xi_l}{\partial x_m} \right]_\kappa + \left[\mathcal{J} \frac{\partial \xi_m}{\partial x_l} \right]_\kappa \mathbf{D}_{\xi_l} \right) \circ \mathbf{F}_{x_m}(\mathbf{q}_\kappa, \mathbf{q}_\kappa) \mathbf{1}_\kappa = \mathbf{SAT}_\kappa^{(1)}, \quad (22)$$

where the symbol \circ indicates the Hadamard product, and $\mathbf{F}_{x_m}(\cdot, \cdot)$ is a two argument matrix flux function which, for an entropy conservative schemes, is constructed from a two-point entropy conservative flux function, $\mathcal{F}_{x_m}^{(1)}(\mathcal{Q}_i, \mathcal{Q}_j)$, (see, for instance, [22]).

Herein, to construct the entropy conservative discretization, we use the two-point entropy conservative flux by Chandrashekar [9] which reads:

$$\mathcal{F}_{x_m}^{(1)}(\mathcal{Q}_i, \mathcal{Q}_j) = \begin{bmatrix} \tilde{\rho} \bar{\mathcal{U}}_m \\ \tilde{\rho} \bar{\mathcal{U}}_m \bar{\mathcal{U}}_1 + \delta_{m,1} \tilde{\mathcal{P}} \\ \tilde{\rho} \bar{\mathcal{U}}_m \bar{\mathcal{U}}_2 + \delta_{m,2} \tilde{\mathcal{P}} \\ \tilde{\rho} \bar{\mathcal{U}}_m \bar{\mathcal{U}}_3 + \delta_{m,3} \tilde{\mathcal{P}} \\ \tilde{\rho} \bar{\mathcal{U}}_m \left(\frac{1}{2(\gamma-1)\beta} - \frac{1}{2} |\bar{\mathcal{U}}|^2 \right) + \bar{\mathcal{U}} \cdot \mathcal{M} \end{bmatrix}, \quad (23)$$

where, for the generic quantity ϕ ,

$$\hat{\phi} = \frac{\phi_i - \phi_j}{\log \phi_i - \log \phi_j}, \quad \bar{\phi} = \frac{\phi_i + \phi_j}{2}$$

are the logarithmic average and the arithmetic average, respectively,

$$\tilde{\mathcal{P}} = R\bar{\rho} \frac{\mathcal{T}_i \mathcal{T}_j}{\bar{\mathcal{T}}}, \quad \beta = \frac{1}{2R\mathcal{T}},$$

and the term \mathcal{M} corresponds to a vector of the three momentum components of this two-point flux. We will refer to our entropy stable discretization as ES-C.

The Hadamard formalism is capable of compactly representing various split forms, and more importantly, extends to nonlinear equations for which a canonical split form is inappropriate. In this work, we also use this formalism to compute the divergence of the inviscid

fluxes using the cheaper two-point flux of Kennedy and Gruber [44]:

$$\mathcal{F}_{x_m}^{(1)}(\mathcal{Q}_i, \mathcal{Q}_j) = \begin{bmatrix} \bar{\rho}\bar{\mathcal{U}}_m \\ \bar{\rho}\bar{\mathcal{U}}_m\bar{\mathcal{U}}_1 + \delta_{m,1}\bar{\mathcal{P}} \\ \bar{\rho}\bar{\mathcal{U}}_m\bar{\mathcal{U}}_2 + \delta_{m,2}\bar{\mathcal{P}} \\ \bar{\rho}\bar{\mathcal{U}}_m\bar{\mathcal{U}}_3 + \delta_{m,3}\bar{\mathcal{P}} \\ \bar{\rho}\bar{\mathcal{U}}_m\bar{\mathcal{E}} + \bar{\mathcal{P}}\bar{\mathcal{U}}_m \end{bmatrix}. \quad (24)$$

We will refer to the discretization that uses the Kennedy and Gruber [44] flux as SF-KG.

Finally, we also compare the above two discretizations with a standard discontinuous collocation type discretization (DC). In this case the divergence of the inviscid fluxes is computed by applying the SBP differentiation matrix to the inviscid flux vector whose components are the direct evaluation of (15) at each node:

$$\mathcal{F}_{x_m}^{(1)}(\mathcal{Q}_i) = [\rho\mathcal{U}_m, \rho\mathcal{U}_m\mathcal{U}_1 + \delta_{m,1}\mathcal{P}, \rho\mathcal{U}_m\mathcal{U}_2 + \delta_{m,2}\mathcal{P}, \rho\mathcal{U}_m\mathcal{U}_3 + \delta_{m,3}\mathcal{P}, \rho\mathcal{P}_m\mathcal{H}]^T. \quad (25)$$

The above flux is the cheapest flux among the fluxes considered herein.

Remark 1. *It is worth noting the differences in the cost of these discretizations. The computing of logarithms contributes significantly to the cost of the inviscid flux evaluations of the entropy stable discretization. Furthermore, the standard DC methods require fewer inviscid flux evaluations than the other two discretizations with $\mathcal{O}(N^3)$ evaluations instead of the $\mathcal{O}(N^4)$ evaluations in the three-dimensional case. Section 5 presents results exploring the differences in the cost of these discretizations.*

Next, recasting the viscous fluxes in terms of entropy variables as shown in eq. (18) yields the following form for the discretization of the divergence of the viscous fluxes

$$\sum_{l,a=1}^3 \frac{\partial}{\partial \xi_l} \left(\hat{\mathcal{C}}_{l,a} \frac{\partial \mathbf{W}}{\partial \xi_a} \right) \approx \sum_{l,a=1}^3 \mathbf{D}_{\xi_l} \left[\hat{\mathcal{C}}_{l,a} \right] \boldsymbol{\theta}_a^\kappa, \quad \boldsymbol{\theta}_a^\kappa = \mathbf{D}_{\xi_a} \mathbf{w}_\kappa. \quad (26)$$

Note that eq. (26) is precisely the symmetric generalization of the convection-diffusion operator to a viscous system.

The discretization on the κ^{th} element reads

$$\mathbf{J}_\kappa \frac{d\mathbf{q}_\kappa}{dt} + \mathbf{I}_\kappa^{(\text{E})} = \sum_{l,a=1}^3 \mathbf{D}_{\xi_a} \left[\widehat{\mathcal{C}}_{l,a} \right] \boldsymbol{\theta}_a^\kappa + \mathbf{SAT}_\kappa^{(1)} + \mathbf{SAT}_\kappa^{(V)} + \mathbf{I}_P^\kappa, \quad \boldsymbol{\theta}_a^\kappa = \mathbf{D}_{\xi_a} \mathbf{w}_\kappa + \mathbf{SAT}_\kappa^\theta, \quad (27)$$

where $\mathbf{I}_\kappa^{(\text{E})}$ represents the discretization of the divergence of the inviscid fluxes and the interior penalty term, \mathbf{I}_P^κ , adds interface dissipation [58]. This term is a design-order zero interface dissipation term that is constructed to damp neutrally stable “odd-even” eigenmodes that arise from the LDG viscous operator. Scheme (27) telescopes to the boundaries where appropriate SATs need to be imposed to obtain a stability statement [56, 60, 79].

5. Numerical results

The curvilinear, unstructured grid, CFD framework used in this article has been developed at the Extreme Computing Research Center (ECRC) at KAUST. The conforming numerical solver is based on the algorithms proposed in [5, 58, 59]. It is built on top of the Portable and Extensible Toolkit for Scientific computing (PETSc) [2], its mesh topology abstraction (DMPLEX) [47] and scalable ordinary differential equation (ODE)/differential algebraic equations (DAE) solver library [1]. The fifth order explicit Runge–Kutta scheme by Dormand and Prince [21] with an adaptive time-stepping based on signal processing [77, 78]) is used to integrate the numerical solution in time. The tolerances of the time integrator used in all test cases are small enough to render the time error negligible.

5.1. Error vs. cost

Convergence studies for 3D flows are conducted, and the serial time to solution is measured. The convergence studies are done on structured cubic domains, using sequences of nested grids. Finally, the L^2 norm of error is calculated using the matrix norm (P-norm) associated with the SBP-SAT scheme.

5.1.1. Inviscid flow: 3D isentropic vortex

Although the focus of this paper is on the compressible Navier–Stokes equations, in this section, we study the propagation of an inviscid 3D isentropic vortex. This first test allows us

to verify and characterize the cost and accuracy of the inviscid component of our algorithm, a key element in any compressible or incompressible Navier–Stokes solver [5, 16, 56].

The simulation of an isentropic vortex is a widely used benchmark problem [74] because it has an analytical solution. In particular, for the stationary case, the exact solution is given by

$$\begin{cases} \rho &= \mathcal{T}^{\frac{1}{\gamma-1}}, \\ \mathcal{U}_t &= \frac{r\beta}{2\pi} \exp\left(\frac{1-r^2}{2}\right), \\ \mathcal{T} &= \mathcal{T}_\infty - \frac{(\gamma-1)\text{Ma}_\infty^2\beta^2}{8\pi^2} \exp(1-r^2), \end{cases} \quad (28)$$

where r is the distance from the axis of the vortex, and \mathcal{U}_t is the tangential velocity. The moving vortex solution is obtained by applying to (28) a uniform translation in the direction of the velocity vector field.

Herein, the simulation domain is a cube $\Omega = [0, 10]^3$ where the vortex rotates around the axis $(1, 1, 1)^T$, a direction not aligned with the grid. A constant velocity field $\mathcal{U}_m = \mathcal{U}_m^\infty$ is imposed and the vortex is simulated for a short amount of time. The parameters for this test are $\gamma = 1.4$, $\text{Ma}_\infty = 0.5$, $\beta = 5$ and $\mathcal{T}_\infty = 1$.

Figure 1 shows the L^2 norm of the error of the density field computed at the final time $t_f = 2.5$ against the serial wall-clock time for the ES-C discretization. We remark that even for large errors, e.g. 10^{-4} , the smallest time to solution is always achieved with high order discretizations (namely $p = 7$ or even $p = 15$).

5.1.2. Viscous flow: 3D manufactured solution

To extend the error vs. cost discussion to the realm of viscous flows, we use the method of manufactured solutions (MMS). The MMS is a powerful technique for code verification widely used in the scientific community [69, 70] where, in principle, the manufactured solution doesn't need to satisfy the PDE under investigation. Here, a proposed smooth solution is inserted into the original PDE so that all derivatives can be calculated analytically. The result is then simplified, and the residual obtained is used as a source term that, once added to the original equation, creates a modified problem for which the analytical solution is known. This solution allows for the comparison between the exact and numerical solutions.

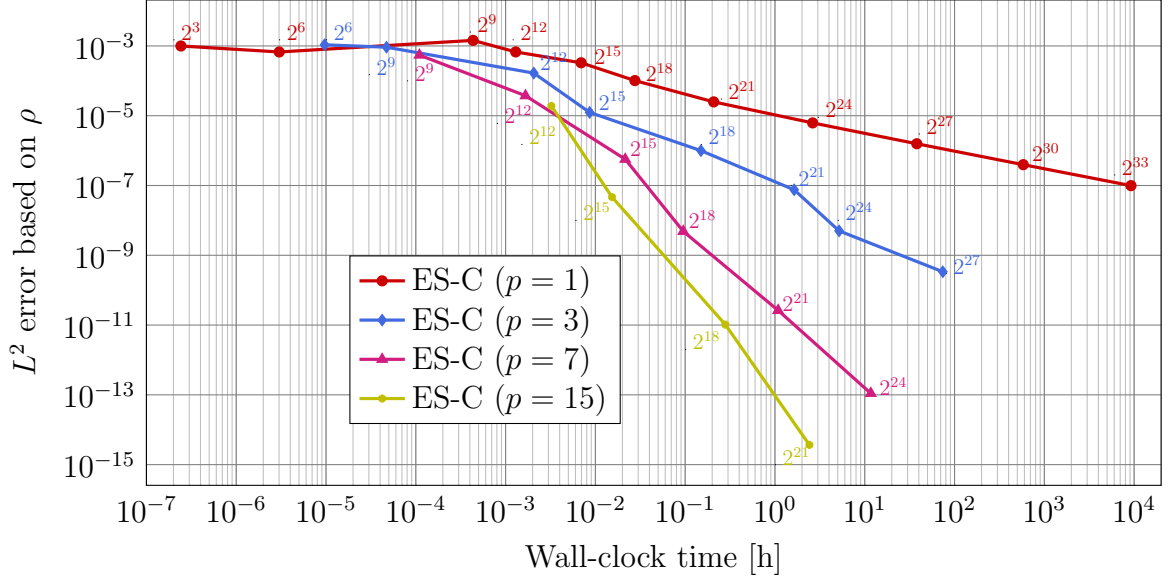


Figure 1: Error vs. cost for the 3D isentropic vortex. The numbers represent the number of degrees of freedom of each simulation.

In this section, this technique is used to evaluate the accuracy versus wall-clock time for different polynomial degrees using both the conventional DC and ES-C discretizations for a supersonic compressible viscous flow. To do so, we consider a cubic domain $\Omega = [0, 1]^3$ with the following manufactured solution

$$\begin{cases}
 \rho &= \rho^0 + \rho^{x_1} \sin\left(\frac{\alpha_{\rho}^{x_1} \pi x_1}{L}\right) + \rho^{x_2} \cos\left(\frac{\alpha_{\rho}^{x_2} \pi x_2}{L}\right) + \rho^{x_3} \sin\left(\frac{\alpha_{\rho}^{x_3} \pi x_3}{L}\right), \\
 \mathcal{U}_1 &= \mathcal{U}_1^0 + \mathcal{U}_1^{x_1} \sin\left(\frac{\alpha_1^{x_1} \pi x_1}{L}\right) + \mathcal{U}_1^{x_2} \cos\left(\frac{\alpha_1^{x_2} \pi x_2}{L}\right) + \mathcal{U}_1^{x_3} \cos\left(\frac{\alpha_1^{x_3} \pi x_3}{L}\right), \\
 \mathcal{U}_2 &= \mathcal{U}_2^0 + \mathcal{U}_2^{x_1} \cos\left(\frac{\alpha_2^{x_1} \pi x_1}{L}\right) + \mathcal{U}_2^{x_2} \sin\left(\frac{\alpha_2^{x_2} \pi x_2}{L}\right) + \mathcal{U}_2^{x_3} \sin\left(\frac{\alpha_2^{x_3} \pi x_3}{L}\right), \\
 \mathcal{U}_3 &= \mathcal{U}_3^0 + \mathcal{U}_3^{x_1} \sin\left(\frac{\alpha_3^{x_1} \pi x_1}{L}\right) + \mathcal{U}_3^{x_2} \sin\left(\frac{\alpha_3^{x_2} \pi x_2}{L}\right) + \mathcal{U}_3^{x_3} \cos\left(\frac{\alpha_3^{x_3} \pi x_3}{L}\right), \\
 \mathcal{P} &= \mathcal{P}^0 + \mathcal{P}^{x_1} \sin\left(\frac{\alpha_{\mathcal{P}}^{x_1} \pi x_1}{L}\right) + \mathcal{P}^{x_2} \sin\left(\frac{\alpha_{\mathcal{P}}^{x_2} \pi x_2}{L}\right) + \mathcal{P}^{x_3} \cos\left(\frac{\alpha_{\mathcal{P}}^{x_3} \pi x_3}{L}\right).
 \end{cases} \quad (29)$$

Expressions (29) are similar to those proposed by Roy [70] and Katz and Sankaran [43]. The constants appearing in this manufactured solution are chosen to give supersonic flow in the three spatial directions (cf. Table 1). Therefore, the exact Dirichlet values for all primitive variables are specified on both inflow and outflow boundaries. The value of the parameters are: $L = 1$, $\gamma = 1.4$, $\text{Re} = 4 \times 10^6$, and $\text{Ma} \approx 2.14$. Figure 2 shows a visualization of this

solution.

Equation, φ	φ^0	φ^{x_1}	φ^{x_2}	φ^{x_3}	$\alpha_\varphi^{x_1}$	$\alpha_\varphi^{x_2}$	$\alpha_\varphi^{x_3}$
ρ	1	3/20	-1/10	1/5	1	1/2	1
\mathcal{U}_1	800	50	-30	50	3/2	3/5	1
\mathcal{U}_2	800	-75	40	10	1/2	3/2	3/2
\mathcal{U}_3	800	15	-25	20	3/2	1/2	5/4
\mathcal{P}	10^5	2×10^4	5×10^4	2/3	1	3/2	1

Table 1: Constants for the 3D compressible Navier–Stokes supersonic manufactured solution.

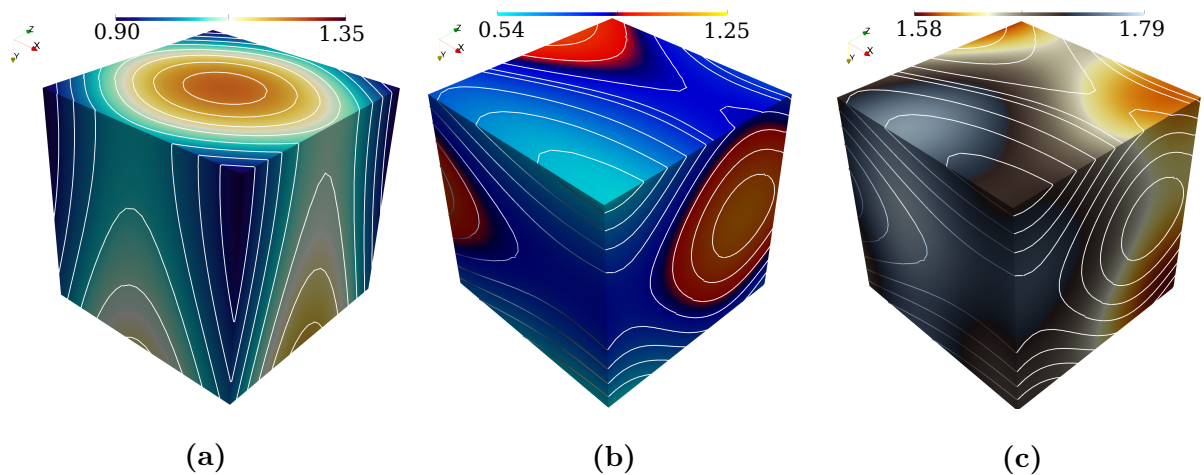


Figure 2: 3D supersonic manufactured solution: (a) density, (b) temperature and (c) velocity magnitude.

Figure 3 shows the results for the L^2 error of the density field against the time to solution for several solution polynomial degrees. The numbers superimposed to the data series represent the total number of degrees of freedom (DOFs) of each mesh, showing that the wall-clock time is almost constant given a total of DOFs, regardless of the polynomial degree. This observation added to the accuracy of high order solutions can result in higher order discretizations being more economical, given some acceptable error threshold. This observation should serve as a motivation to further explore the behavior of high order DC-type discretizations in more applied settings.

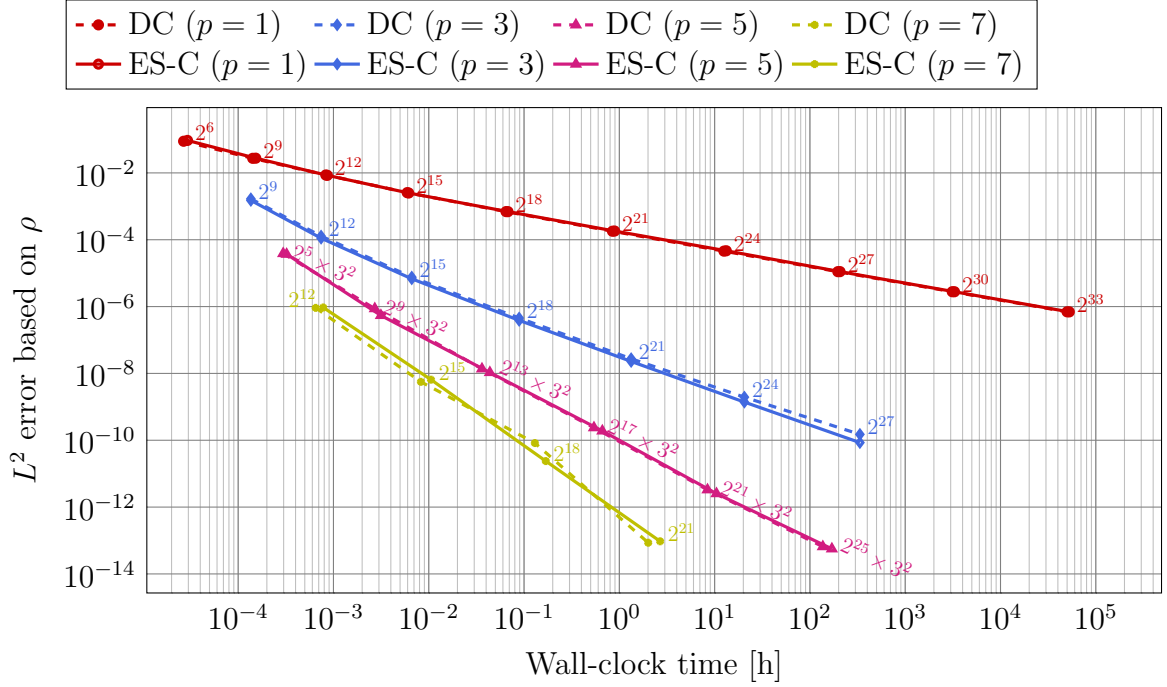


Figure 3: Error vs. cost for 3D manufactured solution.

5.2. The cost of entropy stability

We devised a test to compare the cost of the entropy stable discretization with the non-entropy stable ones. In this test, the Taylor–Green vortex (TGV) at $\text{Re} = 1,600$ and $\text{Ma} = 0.05$ is simulated using a fixed number of DOFs for four different solution polynomial degrees. The initial condition reads

$$\begin{cases}
 \rho &= 1 + \frac{\gamma \text{Ma}^2}{16} (\cos(2x_1) + \cos(2x_2)) (\cos(2x_3) + 2), \\
 \mathcal{U}_1 &= \sin(x_1) \cos(x_2) \cos(x_3), \\
 \mathcal{U}_2 &= -\cos(x_1) \sin(x_2) \cos(x_3), \\
 \mathcal{U}_3 &= 0, \\
 \mathcal{T} &= 1.
 \end{cases} \quad (30)$$

This problem is generally used to study the transition to turbulence, the energy decay in turbulent flow, the simulation of under-resolved turbulent features and the robustness of solvers [14, 34, 51, 57]. Here we use it as a nontrivial flow pattern where we measure the

cost of our discretizations. The mesh is a structured cube domain $\Omega = [-\pi, \pi]^3$ with periodic boundary conditions, discretized with enough elements to guarantee a total of 256 DOFs per direction (for a total of 256^3 DOFs). We use two nodes of Shaheen XC 40 [37] with a perfectly balanced partition⁶. In fact, in our solver, the parallel overhead for this number of nodes is completely negligible. During the execution, a fixed small time step is used and all I/O operations are turned off. The time per time step (TS) is averaged until no noticeable change is observed. The final results are shown in Figure 4.

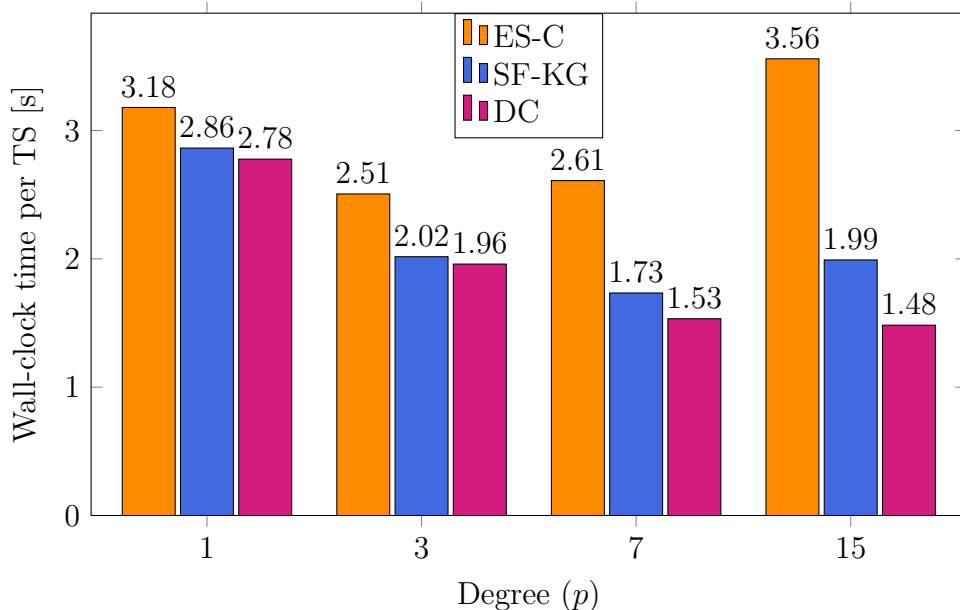


Figure 4: Wall-clock time per time step for different solution polynomial degrees and discretizations.

All the results for wall-clock time per time step fall within the same order of magnitude. This similarity is consistent with the results shown in the Section 5 since the computational cost of the discretization mostly depends on the number of DOFs. The differences within this range are caused by two main factors, namely the number of flux evaluations in the volume terms (with its complexity), and the ratio of the volume terms to the surface terms (SATs). Here the former causes discretizations to be more expensive with increasing polynomial degree, while the latter has the opposite effect. The results for both ES-C and SF-KG

⁶Each Shaheen XC 40 node has 32 Intel Haswell cores.

discretizations show this with a minimum time per time step at $p = 3$ and $p = 7$, respectively, with the SF-KG flux being cheaper. A minimum time per time step for the conventional DC discretization is not found within the studied range of solution polynomial degrees. Obviously, the conventional DC discretization is cheaper because it is characterized by fewer inviscid flux evaluations for all the solution polynomial degree, as discussed in Section 4.

5.3. Robustness

Although high-order accurate methods are well suited for smooth solutions, numerical instabilities may occur if the flow contains *under-resolved physical features* (e.g., under-resolved turbulent flows) or *discontinuities* (e.g., shocks). In this section we investigate the robustness of the three discretizations for under-resolved turbulent and non-smooth flows.

5.3.1. Taylor–Green vortex

The Taylor–Green vortex (TGV) problem at $\text{Re} = 1,600$ and $\text{Ma} = 0.05$ is a flow that degenerates to turbulence over time; therefore its solution is representative of the behavior of the algorithm for the solution of turbulent flows. By simply using coarse grids, this problem can be made a challenging benchmark for the simulation of under-resolved turbulent features, a situation that easily leads to stability issues with high order operators. The study is performed using several nested meshes (see the first column in Table 2) and solution polynomial degrees from $p = 1$ to $p = 15$. The final time is set to $t_f = 20$. Table 2 summarizes the results.

As expected, the DC discretization is frequently unstable and leads to a crash of the solver when coarse meshes with high order solution polynomial degrees are used. On the contrary, the other two methods are always stable. We emphasize that in our test, only the ES-C discretization has a rigorous proof of stability and the particular conditions of the test may be the cause for the perfect score of SF-KG. So it is natural to expect there is a set of problems where even SF-KG is bound to fail. The next section explores further in this difference.

	Degree	1	2	3	4	5	6	7	8	9	10	11	12	13	14	15
ES-C	3^3	✓	✓	✓	✓	✓	✓	✓	✓	✓	✓	✓	✓	✓	✓	✓
	6^3	✓	✓	✓	✓	✓	✓	✓	✓	✓	✓	✓	✓	✓	✓	✓
	12^3	✓	✓	✓	✓	✓	✓	✓	✓	✓	✓	✓	✓	✓	✓	✓
	24^3	✓	✓	✓	✓	✓	✓	✓	✓	✓	✓	✓	✓	✓	✓	✓
	48^3	✓	✓	✓	✓	✓	✓	✓	✓	✓	✓	✓	✓	✓	✓	✓
SF-KG	3^3	✓	✓	✓	✓	✓	✓	✓	✓	✓	✓	✓	✓	✓	✓	✓
	6^3	✓	✓	✓	✓	✓	✓	✓	✓	✓	✓	✓	✓	✓	✓	✓
	12^3	✓	✓	✓	✓	✓	✓	✓	✓	✓	✓	✓	✓	✓	✓	✓
	24^3	✓	✓	✓	✓	✓	✓	✓	✓	✓	✓	✓	✓	✓	✓	✓
	48^3	✓	✓	✓	✓	✓	✓	✓	✓	✓	✓	✓	✓	✓	✓	✓
DC	3^3	✓	✓	×	×	×	×	×	×	×	×	×	×	×	×	×
	6^3	✓	✓	×	×	×	×	×	×	×	×	×	×	×	×	×
	12^3	✓	✓	×	×	×	×	×	×	×	×	×	×	×	×	×
	24^3	✓	✓	✓	×	×	×	×	×	×	✓	×	✓	✓	✓	✓
	48^3	✓	✓	✓	✓	×	×	✓	✓	✓	✓	✓	✓	✓	✓	✓
	96^3	✓	✓	✓	✓	✓	✓	✓	✓	–	–	–	–	–	–	–

Table 2: Numerical stability for the 3D Taylor–Green vortex. ✓ = success, × = failure.

5.3.2. Compressible homogeneous isotropic turbulence

We select this 3D case as a more challenging problem to further stress the stability properties of our discretizations. This problem is regarded as one of the cornerstones to elucidate the effects of compressibility for compressible turbulence [49]. Based on the previous numerical experiments and theoretical analyses, isotropic compressible turbulence is divided into four main dynamical regimes [71], i.e., the low-Mach number quasi-isentropic regime, the low-Mach number thermal regime, the nonlinear subsonic regime, and the supersonic regime. Most of the numerical schemes developed in the last decade utilized in the simulation of isotropic compressible turbulence with moderate turbulent Mach number to supersonic regimes fail to capture shocklets robustly and accurately resolve smooth regions. For isotropic compressible turbulence in these two regimes, the stronger random shocklets and higher spatial-temporal gradients pose greater difficulties for numerical analyses than other regimes. Both forced isotropic compressible turbulence with solenoidal and dilatational external force [42, 45] and decaying isotropic compressible turbulence [4, 63, 72] are studied in the literature. In this paper, we choose to test with the decaying isotropic compressible

turbulence without external force. The flow domain of numerical simulation is a cube box defined as $\Omega = [0, 2\pi]^3$, with periodic boundary conditions in all directions. The evolution of this artificial system is determined by initial thermodynamic quantities and two dimensionless parameters, i.e., the initial Taylor microscale Reynolds number $\text{Re} = \langle \rho \rangle \mathcal{U}_{\text{RMS}} \lambda / \langle \mu \rangle$, and turbulent Mach number $\text{Ma}_t = \mathcal{U}_{\text{RMS}} / \langle c_s \rangle$, where $\langle \cdot \rangle$ is the ensemble over the whole computational domain, ρ is the density, μ is the initial dynamic viscosity, c_s is the sound speed, \mathcal{U}_{RMS} is the root mean square of initial turbulent velocity field $\mathcal{U}_{\text{RMS}} = \langle \mathcal{U} \cdot \mathcal{U} / 3 \rangle^{1/2}$, and the normalized Taylor micro-scale λ is defined by

$$\lambda = \sqrt{\frac{\mathcal{U}_{\text{RMS}}}{\left\langle \left(\frac{\partial \mathcal{U}_1}{\partial x_1} \right)^2 + \left(\frac{\partial \mathcal{U}_2}{\partial x_2} \right)^2 + \left(\frac{\partial \mathcal{U}_3}{\partial x_3} \right)^2 \right\rangle}}. \quad (31)$$

A 3D solenoidal random initial velocity field \mathcal{U} can be generated by a specified spectrum, which is given by [61]

$$E(k) = A_0 k^4 \exp(-2k^2/k_0^2), \quad (32)$$

where A_0 is a constant to get a specified initial kinetic energy, k is the wave number, k_0 is the wave number at which the spectrum peaks. In this paper, fixed A_0 and k_0 in Equation (32) are chosen for all cases, which are initialized by $A_0 = 0.00013$ and $k_0 = 8$. Initial strategies play an important role in isotropic compressible turbulence simulation [72], especially for the starting fast transient period during which the divergence of the velocity increases rapidly and negative temperature or pressure often appear. In the computation, the initial pressure \mathcal{P}_0 , density ρ_0 and temperature \mathcal{T}_0 are set following the procedure of Ristorcelli and Blaisdell [68]. For higher polynomial degree, the hydrodynamic and thermodynamic fields are computed from polynomial order $p = 1$ and then mapped onto the particular grid. Simulations are run for a relatively short time interval which is the three order of magnitude of a characteristic eddy turnover time $\tau = \mathcal{L}_1 / \mathcal{U}_{\text{RMS}}$ where \mathcal{L}_1 being the integral length scale defined as

$$\mathcal{L}_1 = \frac{3\pi}{4} \frac{\int_0^\infty E(k) dk / k}{\int_0^\infty E(k) dk}. \quad (33)$$

To assess the relative robustness of the discretizations, the turbulent Mach number is set to $\text{Ma}_t = 0.62$, where shocklets appear and thus the flow belong to the nonlinear subsonic

regime in which compressible effects are important. The number of wavenumber available in the computational box is intentionally limited to values that do not allow a correct representation of the smallest scales of the initially imposed turbulent field. In all flow simulations the turbulent Reynolds number is $\text{Re}_\lambda = 194$.

Several test runs at multiple resolutions and polynomial orders are performed to assess the numerical robustness of the conventional DC, SF-KG and ES-C schemes.

	Degree	1	2	3	4
ES-C	4^3	✓	✓	✓	✓
	8^3	✓	✓	✓	✓
	16^3	✓	✓	✓	✓
	32^3	✓	✓	✓	✓
	64^3	✓	✓	✓	✓
SF-KG	4^3	×	✓	✓	✓
	8^3	×	✓	✓	✓
	16^3	×	✓	✓	✓
	32^3	×	✓	✓	✓
	64^3	✓	✓	✓	✓
DC	4^3	×	×	×	×
	8^3	×	×	×	×
	16^3	×	×	×	✓
	32^3	×	×	✓	✓
	64^3	✓	✓	✓	✓

Table 3: Numerical stability for the compressible homogeneous isotropic turbulence at $\text{Re}_\lambda = 194$ and $\text{Ma}_t = 0.62$. ✓ = success, × = failure.

As summarized in Table 3, only the ES-C scheme shows the numerical robustness to compute this flow for all the selected meshes and solution polynomial degree and produce results past the initial start-up phase. The conventional DC algorithm is numerically unstable at lower resolution at all polynomial orders, while SF-KG crashes if a polynomial order of $p = 1$ is used for a mesh resolution up to 32^3 .

Figure 5 shows both the decaying history of the resolved turbulent kinetic energy $\mathcal{E}_K = \langle \rho \mathcal{U}_i \mathcal{U}_i \rangle / 2$ versus t/τ and Reynolds number based on Taylor micro-scale versus t/τ for the different schemes and polynomial order $p = 1$, where the dashed lines indicate the points of termination (crash).

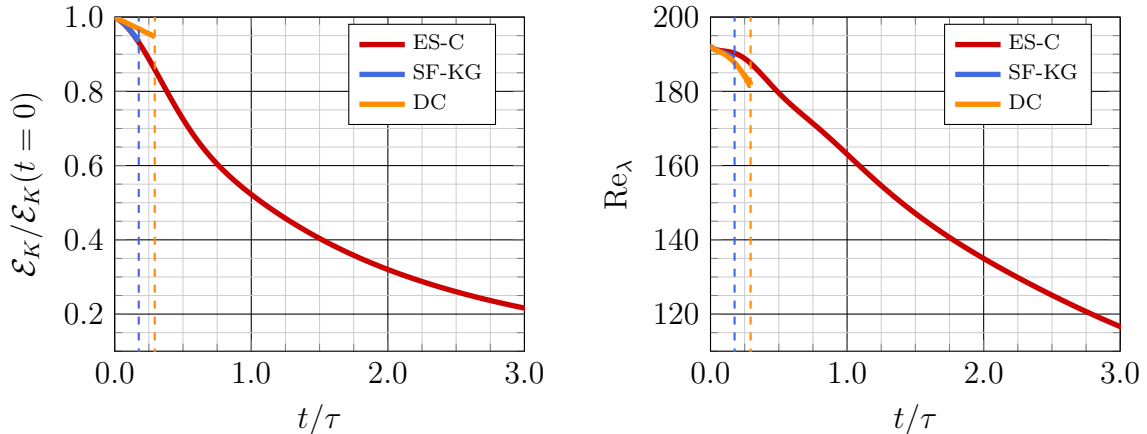


Figure 5: Compressible isotropic turbulence at $\text{Re}_\lambda = 194$ and $\text{Ma}_t = 0.62$. The points of termination are indicated by dashed lines.

In Figure 6, the path lines on the boundaries are plotted at two instants for the ES-C scheme using the line integral convolution colored by the magnitude of the velocity. As expected, the velocity field at $t/\tau = 3$ clearly contains more small scales than the initial field $t/\tau = 2$, which shows the need to use a numerically robust scheme to capture them without filtering and also to properly handle shocklets that quickly form for such a higher turbulent Mach number. It is concluded from this test case that numerical schemes which are entropy stable are more desirable for such a highly strong Mach-number regime. In fact, schemes that satisfy entropy condition are found to lead to stable density fluctuations in compressible isotropic turbulence simulations, while schemes that do not have this property can be unstable with respect to density fluctuations [40, 63].

5.3.3. Supersonic turbulent flows past a bar

The last test we present is the 3D supersonic flow around a square bar, a problem that has been studied in depth in the literature related to supersonic flow around bluff bodies [3, 52, 59]. The similarity parameters are $\text{Re}_\infty = 10,000$ and $\text{Ma}_\infty = 1.5$. In this regime the flow exhibits a complicated pattern characterized by shocks, expansion zones and separation [59]. This test is chosen as a challenging problem to stress the robustness of our discretizations in the context of supersonic turbulent flow.

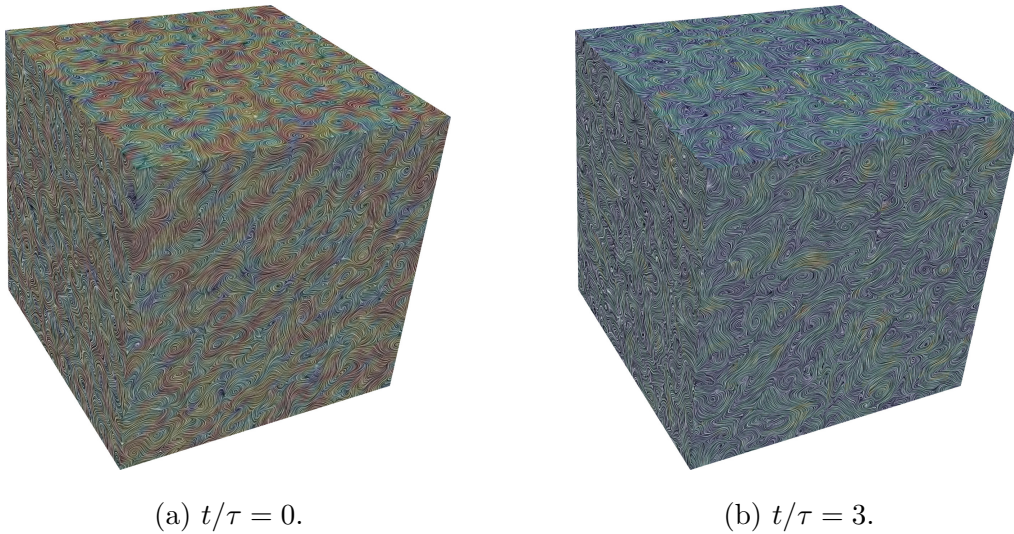


Figure 6: Path lines on the surface of velocity field from ES-C with $p = 9$ using 32^3 for the compressible isotropic turbulence at $\text{Re}_\lambda = 194$ and $\text{Ma}_t = 0.62$.

A 3D square of unit side is placed at the origin of the system of reference and an unstructured quad mesh with refinement is extended out to a box 20 and 50 length units in the upstream and downstream directions, respectively, 25 length units in both normal directions to the bar, and then extruded one length unit in the spanwise direction. Figure 8 shows the resulting mesh with refinements around the shocks and the turbulent wake; we choose a polynomial degree of $p = 3$ as a reasonable accuracy for this mesh. The boundary conditions used are adiabatic wall on the surface of the bar [13, 59], periodic in the spanwise direction and farfield on the remaining boundaries. The initial condition is set to be a uniform supersonic flow. The simulation run until the main bow shock stabilizes.

Figure 7 shows the results for the pressure drag coefficient ($C_d^{(P)}$) and the viscous drag coefficient ($C_d^{(V)}$) for the initial time steps for the ES-C and the SF-KG discretizations. The dashed line indicates the termination time due to the solver crash. Here the the DC discretization crashed very early in the simulation ($t \approx 1.3 \times 10^{-3}$) yielding no useful results.

Figure 9 shows a visualization of the last recorded step of the solution given by SF-KG (right side), compared with ES-C (left) at the same time. This result is very early in the simulation when the shock propagating from the leading edge is still close to the wall. Here

we choose color schemes intended to highlight the differences between the two simulations, particularly in the shock region where the (expected) oscillations appear to be more regular for the ES-C case. We remark that this visualization has no evidence for the onset of numerical instability; even though SF-KG immediately crashes at the next time step.

Figure 10 shows the resulting flow pattern for the ES-C discretization at $t = 100$.

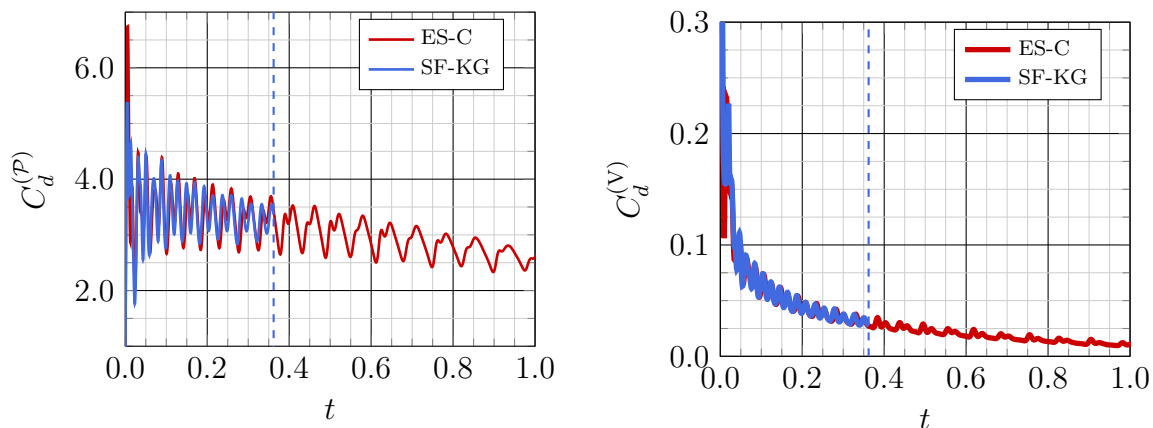


Figure 7: Drag coefficient for the supersonic bar at $\text{Re}_\infty = 10,000$ and $\text{Ma}_\infty = 1.5$.

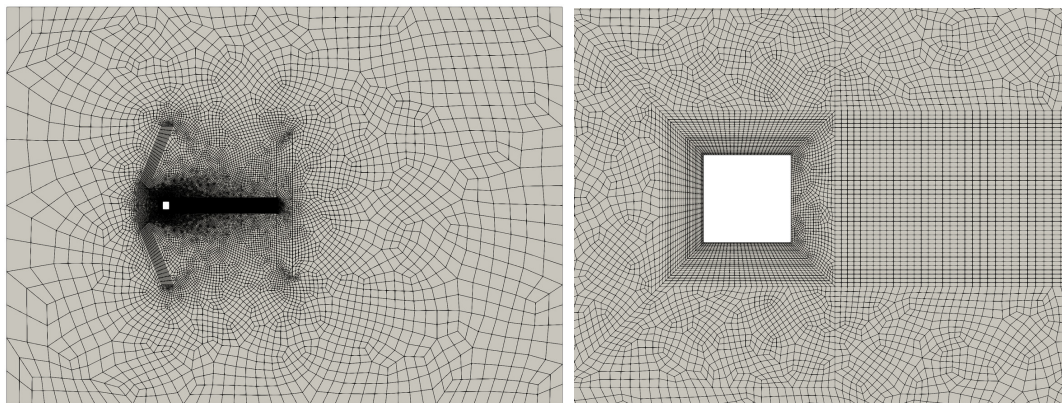
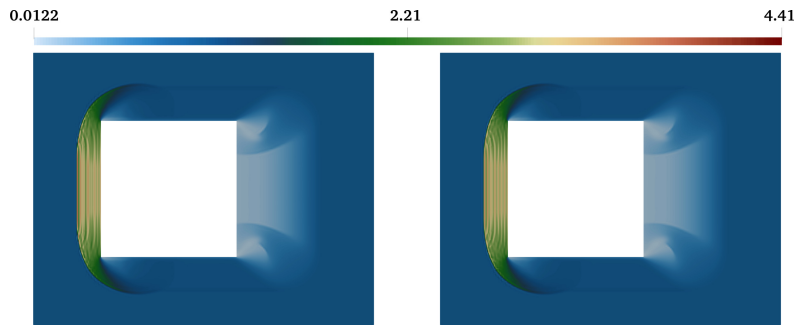


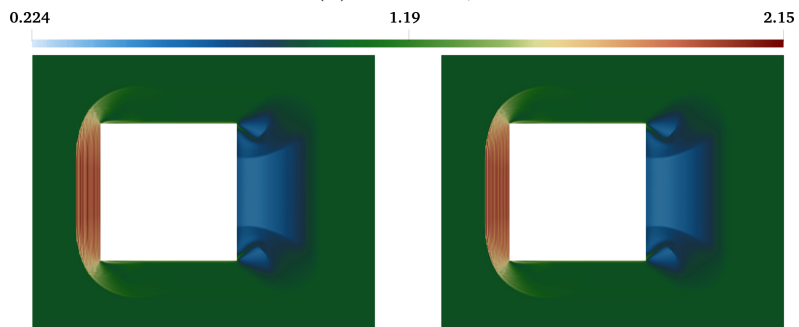
Figure 8: Bi-dimensional view of (left) the 3D mesh used for the supersonic flow around a square bar and (right) zoom at the square bar.

6. Conclusion

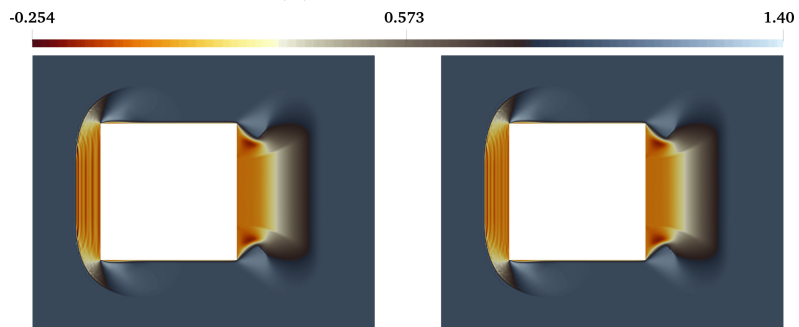
This work presents a three-way comparison between one entropy stable, and two non-entropy stable discretizations, in the context of split form and discontinuous collocation



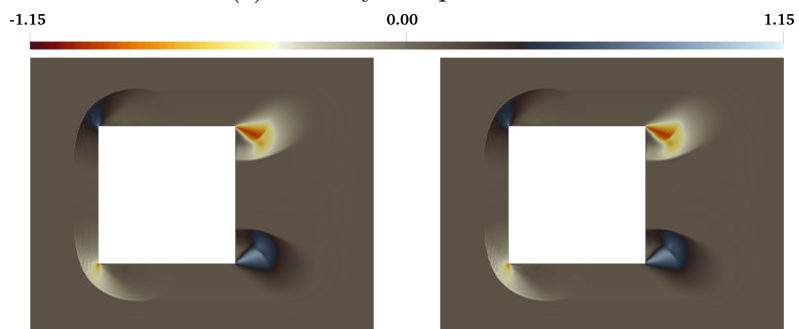
(a) Density ρ .



(b) Temperature \mathcal{T} .



(c) Velocity component \mathcal{U}_1 .



(d) Velocity component \mathcal{U}_2 .

Figure 9: Comparison of the last recorded step for SF-KG (right) and ES-C (left) at $t = 0.36$ for the supersonic bar at $\text{Re}_\infty = 10,000$ and $\text{Ma}_\infty = 1.5$.

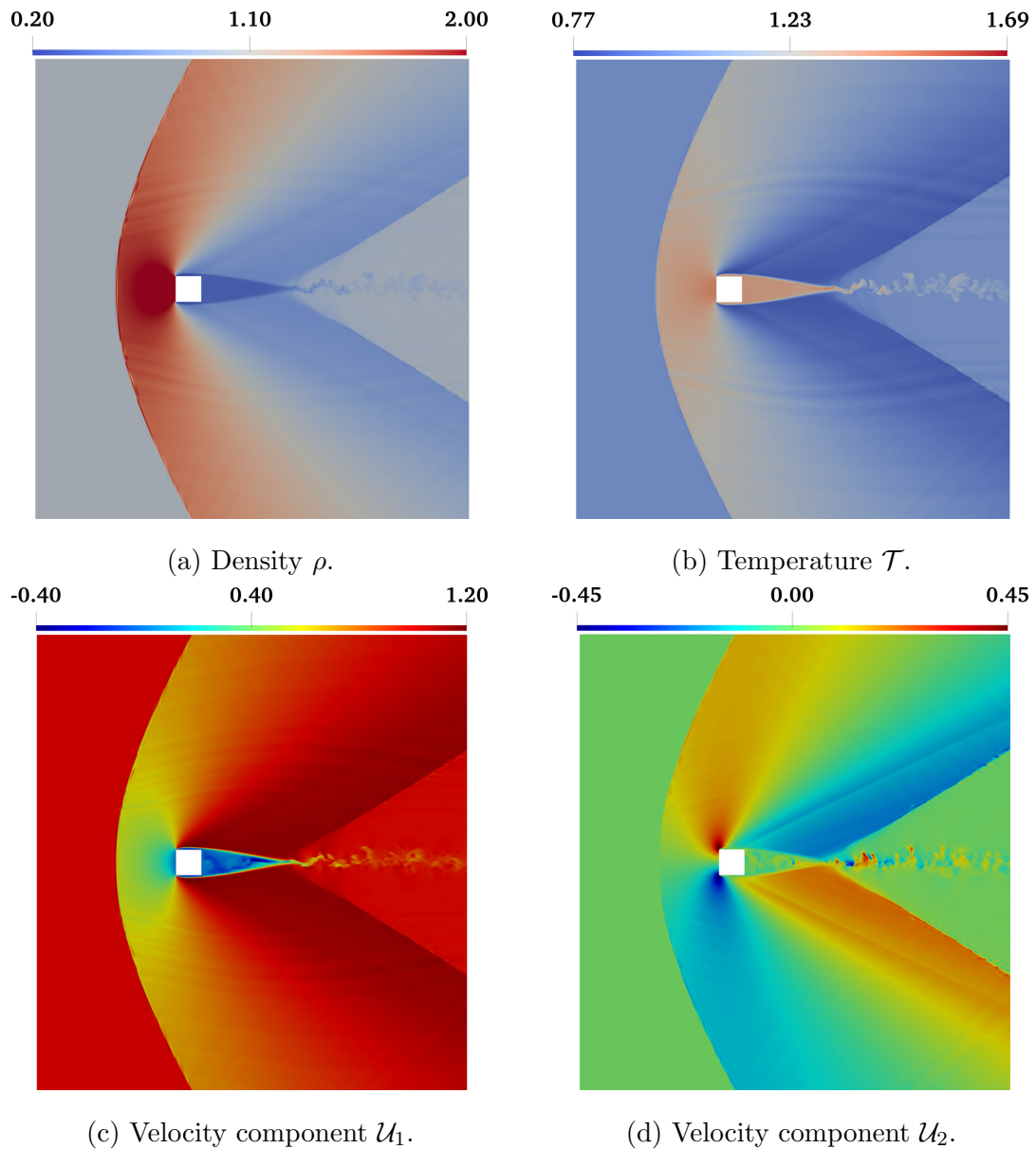


Figure 10: Instantaneous snapshots of fields at $t = 130$ for the supersonic bar at $\text{Re}_\infty = 10,000$ and $\text{Ma}_\infty = 1.5$.

discretizations for the simulation of the compressible Navier–Stokes equations. All three algorithms are constructed using SBP–SAT operators. The entropy stable discretization is based on the two-point entropy conservative flux of Chandrashekar [9], the kinetic energy preserving but not entropy stable discretization is built using the splitting of Kennedy and Gruber [44], and the conventional discontinuous collocation method is based on the standard

inviscid flux arising from the compressible Euler equations.

We have started our discussion with a note on the potential superiority of high order discretizations, not only measured in terms of accuracy but also in wall-clock time for the propagation of a 3D isentropic vortex and a 3D supersonic flow constructed with the method of manufactured solutions. Subsequently, by using the Taylor–Green vortex problem, we have shown the impact of the solution polynomial degree on the computational cost of the three discretizations. In DC-type discretizations, the computational cost depends on the number of flux evaluations (multiplied by its computational complexity), and the cost of computing the surface terms (SATs). These costs have opposite behaviors as the polynomial degree increases and therefore, an optimal wall-clock time per time step can be found. The overall observation is that higher degrees ($p = 3$ or higher) yield the lowest wall-clock time per time step. This superiority is of paramount importance in the implementation of such simulation tools for current and future computing hardware. Hence, the emphasis is placed on higher-order discretizations throughout the entire paper.

We then moved on to the analysis of the reliability and robustness of the three discretizations under three stressful experimental conditions: i) turbulent flows with under-resolved features, ii) shocklets in compressible turbulent flow, and iii) shocks in supersonic flow. As expected, only the entropy stable discretization is able to simulate all test cases successfully. This robustness comes at a cost, which we consider to be affordable for reasonably high-order discretizations (p up to 7), especially in large-scale complex simulations where any instability is unacceptable. We interpret these results as significant evidence in favor of the applicability of entropy stable discretizations in future CFD solvers as reported in [76].

We expect to see future extensions to this work addressing more applied aspects of the implementation of entropy stable discretizations such as performance at scale and hp -refinement, to name a few.

Acknowledgments

The research reported in this paper was funded by King Abdullah University of Science and Technology. We are thankful for the computing resources of the Supercomputing Labo-

ratory and the Extreme Computing Research Center at King Abdullah University of Science and Technology.

References

- [1] Abhyankar, S., Brown, J., Constantinescu, E. M., Ghosh, D., Smith, B. F., and Zhang, H. (2018). PETSc/TS: A modern scalable ODE/DAE solver library.
- [2] Balay, S., Abhyankar, S., Adams, M. F., Brown, J., Brune, P., Buschelman, K., Dalcin, L., Dener, A., Eijkhout, V., Gropp, W. D., Kaushik, D., Knepley, M. G., May, D. A., McInnes, L. C., Mills, R. T., Munson, T., Rupp, K., Sanan, P., Smith, B. F., Zampini, S., Zhang, H., and Zhang, H. (2018). PETSc users manual. Technical Report ANL-95/11 - Revision 3.10, Argonne National Laboratory.
- [3] Birch, T. J., Prince, S. A., and Simpson, G. M. (2003). An experimental and computational study of the aerodynamics of a square cross-section body at supersonic speeds. Technical report, Defence Evaluation and Research Agency.
- [4] Boukharfane, R. (2018). *Contribution à la simulation numérique d'écoulements turbulents compressibles canoniques*. PhD thesis, Chasseneuil-du-Poitou, École Nationale Supérieure de Mécanique et d'Aérotechnique.
- [5] Carpenter, M. H., Fisher, T., Nielsen, E., and Frankel, S. (2014). Entropy stable spectral collocation schemes for the Navier–Stokes equations: Discontinuous interfaces. *SIAM Journal on Scientific Computing*, 36(5):B835–B867.
- [6] Carpenter, M. H., Parsani, M., Fisher, T. C., and Nielsen, E. J. (2015). Entropy stable staggered grid spectral collocation for the Burgers' and the compressible Navier–Stokes equations. *NASA TM-2015-218990*.
- [7] Carpenter, M. H., Parsani, M., Nielsen, E. J., and Fisher, T. C. (2016). Towards an entropy stable spectral element framework for computational fluid dynamics. In *54th AIAA Aerospace Sciences Meeting*, AIAA 2016-1058. American Institute of Aeronautics and Astronautics.
- [8] Chan, J. (2018). On discretely entropy conservative and entropy stable discontinuous Galerkin methods. *Journal of Computational Physics*, 362:346 – 374.
- [9] Chandrashekar, P. (2013). Kinetic energy preserving and entropy stable finite volume schemes for compressible euler and navier-stokes equations. *Communications in Computational Physics*, 14(5):1252–1286.
- [10] Chen, T. and Shu, C.-W. (2017). Entropy stable high order discontinuous Galerkin methods with suitable quadrature rules for hyperbolic conservation laws. *Journal of Computational Physics*, 345:427 – 461.

- [11] Crean, J., Hicken, J. E., Del Rey Fernández, D. C., Zingg, D. W., and Carpenter, M. H. (2018). Entropy-stable summation-by-parts discretization of the Euler equations on general curved elements. *Journal of Computational Physics*, 356:410 – 438.
- [12] Dafermos, C. M. (2010). *Hyperbolic conservation laws in continuum physics*. Springer-Verlag, Berlin.
- [13] Dalcin, L., Rojas, D., Zampini, S., Del Rey Fernández, D. C., Carpenter, M. H., and Parsani, M. (2019). Conservative and entropy stable solid wall boundary conditions for the compressible Navier–Stokes equations: Adiabatic wall and heat entropy transfer. *Journal of Computational Physics*, 397:108775.
- [14] DeBonis, J. (2013). Solutions of the Taylor–Green vortex problem using high-resolution explicit finite difference methods. In *51st AIAA Aerospace Sciences Meeting including the New Horizons Forum and Aerospace Exposition*, page 382.
- [15] Del Rey Fernández, D. C., Boom, P. D., and Zingg, D. W. (2014a). A generalized framework for nodal first derivative summation-by-parts operators. *Journal of Computational Physics*, 266(1):214–239.
- [16] Del Rey Fernández, D. C., Carpenter, M. H., Dalcin, L., Fredrich, L., Winters, A. R., Gassner, G. J., Zampini, S., and Parsani, M. (2019b). Entropy stable p –nonconforming discretizations with the summation-by-parts property for the compressible Euler equations. *Submitted to SIAM Journal of Scientific Computing*.
- [17] Del Rey Fernández, D. C., Carpenter, M. H., Dalcin, L., Fredrich, L., Winters, A. R., Gassner, G. J., Zampini, S., and Parsani, M. (2019a). Entropy stable p –nonconforming discretizations with the summation-by-parts property for the compressible Navier–Stokes equations. *Submitted to Computer & Fluids*.
- [18] Del Rey Fernández, D. C., Carpenter, M. H., Dalcin, L., Zampini, S., and Parsani, M. (2019c). Entropy stable h/p non-conforming discretization with the summation-by-parts property for the compressible Euler and Navier–Stokes equations. Submitted to SN Partial Differential Equations and Applications.
- [19] Del Rey Fernández, D. C., Crean, J., Carpenter, M. H., and Hicken, J. E. (2019d). Staggered entropy-stable summation-by-parts discretization of the Euler equations on general curved elements. *Journal of Computational Physics*, 392:161–186.
- [20] Del Rey Fernández, D. C., Hicken, J. E., and Zingg, D. W. (2014b). Review of summation-by-parts operators with simultaneous approximation terms for the numerical solution of partial differential equations. *Computers & Fluids*, 95(22):171–196.
- [21] Dormand, J. and Prince, P. (1980). A family of embedded Runge–Kutta formulae. *Journal of Computational and Applied Mathematics*, 6(1):19 – 26.
- [22] Fernández, D. C., Carpenter, M. H., Dalcin, L., Fredrich, L., Rojas, D., Winters, A. R., Gassner, G. J., Zampini, S., and Parsani, M. (2019). Entropy stable non-conforming discretizations with the summation-by-parts property for curvilinear coordinates. *NASA TM-2019-*.

- [23] Fernandez, D. C., Carpenter, M. H., Dalcin, L., Fredrich, L., Rojas, D., Winters, A. R., Gassner, G. J., Zampini, S., and Parsani, M. (2019). Entropy stable p -nonconforming discretizations with the summation-by-parts property for the compressible Euler equations.
- [24] Fisher, T. C. (2012). *High-order L^2 stable multi-domain finite difference method for compressible flows*. PhD thesis, Purdue University.
- [25] Fisher, T. C. and Carpenter, M. H. (2013). High-order entropy stable finite difference schemes for nonlinear conservation laws: Finite domains. *Journal of Computational Physics*, 252:518–557.
- [26] Fisher, T. C., Carpenter, M. H., Nordström, J., and Yamaleev, N. K. (2013). Discretely conservative finite-difference formulations for nonlinear conservation laws in split form: Theory and boundary conditions. *Journal of Computational Physics*, 234(1):353–375.
- [27] Fjordholm, U. S., Mishra, S., and Tadmor, E. (2012). Arbitrarily high-order accurate entropy stable essentially nonoscillatory schemes for systems of conservation laws. *Communications in Computational Physics*, 50(2):554–573.
- [28] Flad, D. and Gassner, G. J. (2017). On the use of kinetic energy preserving DG-schemes for large eddy simulation. *Journal of Computational Physics*, 350:782–795.
- [29] Friedrich, L., Shnücke, G., Winters, A. R., Del Rey Fernández, D. C., Gassner, G. J., and Carpenter, M. H. (2019). Entropy stable space-time discontinuous Galerkin schemes with summation-by-parts property for hyperbolic conservation laws. *Journal of Scientific Computing*, 80(1):175–222.
- [30] Friedrich, L., Winters, A. R., Del Rey Fernández, D. C., Gassner, G. J., Parsani, M., and Carpenter, M. H. (2018). An entropy stable h/p non-conforming discontinuous Galerkin method with the summation-by-parts property. *Journal of Scientific Computing*, 77(2).
- [31] Gassner, G. J. (2013). A skew-symmetric discontinuous Galerkin spectral element discretization and its relation to SBP-SAT finite difference methods. *SIAM Journal on Scientific Computing*, 35(3):A1233–A1253.
- [32] Gassner, G. J. and Beck, A. D. (2013). On the accuracy of high-order discretizations for underresolved turbulence simulations. *Theoretical and Computational Fluid Dynamics*, 27(3):221–237.
- [33] Gassner, G. J., Winters, A. R., and Kopriva, D. A. (2016a). Split form nodal discontinuous Galerkin schemes with summation-by-parts property for the compressible Euler equations. *Journal of Computational Physics*, 327:39 – 66.
- [34] Gassner, G. J., Winters, A. R., and Kopriva, D. A. (2016b). Split form nodal discontinuous Galerkin schemes with summation-by-parts property for the compressible Euler equations. *Journal of Computational Physics*, 327(C):39–66.
- [35] Gassner, G. J., Winters, A. R., and Kopriva, D. A. (2016c). A well balanced and entropy conservative discontinuous Galerkin spectral element method for the shallow water equations. *Applied Mathematics and*

- Computation*, 272:291 – 308. Recent Advances in Numerical Methods for Hyperbolic Partial Differential Equations.
- [36] Gerritsen, M. and Olsson, P. (1996). Designing an efficient solution strategy for fluid flows 1. A stable high order finite difference scheme and sharp shock resolution for the Euler equations. *Journal of Computational Physics*, 129(2):245–262.
- [37] Hadri, B., Kortas, S., Feki, S., Khurram, R., and Newby, G. (2015). Overview of the KAUST’s Cray X40 System – Shaheen II. *Proceedings of the Cray User Group Meeting*.
- [Hadri et al.] Hadri, B., Parsani, M., Hutchinson, M., Heinecke, A., Dalcin, L., and Keyes, D. Performance study of sustained petascale direct numerical simulation on Cray XC40 systems (Trinity, Shaheen2 and Cori). *Concurrency and Computation: Practice and Experience*.
- [39] Hesthaven, J. S. and Warburton, T. (2008). *Nodal discontinuous Galerkin methods: Algorithms, analysis, and applications*. Texts in Applied Mathematics. Springer.
- [40] Honein, A. E. and Moin, P. (2004). Higher entropy conservation and numerical stability of compressible turbulence simulations. *Journal of Computational Physics*, 201(2):531–545.
- [41] Hughes, T. J. R., Franca, L. P., and Mallet, M. (1986). A new finite element formulation for computational fluid dynamics, I: symmetric forms of the compressible Navier–Stokes equations and the second law of thermodynamics. *Computer Methods in Applied Mechanics and Engineering*, 54(2):223 – 234.
- [42] Jagannathan, S. and Donzis, D. A. (2016). Reynolds and mach number scaling in solenoidally-forced compressible turbulence using high-resolution direct numerical simulations. *Journal of Fluid Mechanics*, 789:669–707.
- [43] Katz, A. and Sankaran, V. (2011). Mesh quality effects on the accuracy of cfd solutions on unstructured meshes. *Journal of Computational Physics*, 230(20):7670–7686.
- [44] Kennedy, C. A. and Gruber, A. (2008). Reduced aliasing formulations of the convective terms within the Navier–Stokes equations for a compressible fluid. *Journal of Computational Physics*, 227(3):1676–1700.
- [45] Kida, S. and Orszag, S. A. (1990). Energy and spectral dynamics in forced compressible turbulence. *Journal of Scientific Computing*, 5(2):85–125.
- [46] Klose, B. F., Jacobs, G. B., and Kopriva, D. A. (2019). On the robustness and accuracy of marginally resolved discontinuous Galerkin schemes for two dimensional Navier–Stokes flows. In *AIAA Scitech 2019 Forum*, page 0780. American Institute of Aeronautics and Astronautics.
- [47] Knepley, M. G. and Karpeev, D. A. (2009). Mesh algorithms for PDE with Sieve I: Mesh distribution. *Scientific Programming*, 17(3):215–230.
- [48] Kreiss, H.-O. and Scherer, G. (1974). Finite element and finite difference methods for hyperbolic partial differential equations. In de Boor, C., editor, *Mathematical Aspects of Finite Elements in Partial Differential Equations*, pages 195–212, New York. Academic Press.

- [49] Lele, S. K. (1994). Compressibility effects on turbulence. *Annual Review of Fluid Mechanics*, 26(1):211–254.
- [50] Mengaldo, G., De Grazia, D., Moxey, D., Vincent, P., and Sherwin, S. (2015). Dealiasing techniques for high-order spectral element methods on regular and irregular grids. *Journal of Computational Physics*, 299:56–81.
- [51] Moura, R., Sherwin, S., and Peiro, J. (2015). On dg-based iles approaches at very high reynolds numbers. *Report, Research Gate*.
- [52] Nakagawa, T. (1988). Effects of an airfoil and shock waves on vortex shedding process behind a square cylinder. *Acta mechanica*, 72(1-2):131–146.
- [53] Nolasco, I. R., Dalcin, L., Del Rey Fernández, D. C., Zampini, S., and Parsani, M. (2019). Optimized geometrical metrics satisfying free-stream preservation. *Submitted to Computer & Fluids*.
- [54] Nordström, J. and Björck, M. (2001). Finite volume approximations and strict stability for hyperbolic problems. *Applied Numerical Mathematics*, 38(3):237–255.
- [55] Olsson, P. and Olinger, J. (1994). Energy and maximum norm estimates for nonlinear conservation laws. Technical Report 94–01, The Research Institute of Advanced Computer Science.
- [56] Parsani, M., Carpenter, M. H., Fisher, T., and Nielsen, E. (2016a). Entropy stable staggered grid discontinuous spectral collocation methods of any order for the compressible Navier–Stokes equations. *SIAM Journal on Scientific Computing*, 38(5):A3129–A3162.
- [57] Parsani, M., Carpenter, M. H., Fisher, T. C., and Nielsen, E. J. (2016b). Entropy stable staggered grid discontinuous spectral collocation methods of any order for the compressible Navier–Stokes equations. *SIAM Journal on Scientific Computing*, 38(5):A3129–A3162.
- [58] Parsani, M., Carpenter, M. H., and Nielsen, E. J. (2015a). Entropy stable discontinuous interfaces coupling for the three-dimensional compressible Navier–Stokes equations. *Journal of Computational Physics*, 290:132–138.
- [59] Parsani, M., Carpenter, M. H., and Nielsen, E. J. (2015b). Entropy stable wall boundary conditions for the three-dimensional compressible Navier–Stokes equations. *Journal of Computational Physics*, 292:88–113.
- [60] Parsani, M., Carpenter, M. H., and Nielsen, E. J. (2015c). Entropy stable wall boundary conditions for the three-dimensional compressible Navier–Stokes equations. *Journal of Computational Physics*, 292(1):88–113.
- [61] Passot, T. and Pouquet, A. (1987). Numerical simulation of compressible homogeneous flows in the turbulent regime. *Journal of Fluid Mechanics*, 181:441–466.
- [62] Pazner, W. and Persson, P.-O. (2019). Analysis and entropy stability of the line-based discontinuous Galerkin method. *Journal of Scientific Computing*, 80(1):376–402.

- [63] Pirozzoli, S. and Grasso, F. (2004). Direct numerical simulations of isotropic compressible turbulence: influence of compressibility on dynamics and structures. *Physics of Fluids*, 16(12):4386–4407.
- [64] Ranocha, H. (2019). Mimetic properties of difference operators: Product and chain rules as for functions of bounded variation and entropy stability of second derivatives. *BIT Numerical Mathematics*, 59(2):547–563.
- [65] Ranocha, H., Öffner, P., and Sonar, T. (2016). Summation-by-parts operators for correction procedure via reconstruction. *Journal of Computational Physics*, 311:299–328.
- [66] Ranocha, H., Sayyari, M., Dalcin, L., Parsani, M., and Ketcheson, D. I. (2019). Relaxation Runge–Kutta methods: Fully-discrete explicit entropy-stable schemes for the Euler and Navier–Stokes equations. Accepted in *SIAM Journal on Scientific Computing*.
- [67] Ray, D., Chandrashekar, P., Fjordhom, U. S., and Mishra, S. (2016). Entropy stable scheme on two-dimensional unstructured grids for Euler equations. *Communications in Computational Physics*, 19(5):1111–1140.
- [68] Ristorcelli, J. R. and Blaisdell, G. A. (1997). Consistent initial conditions for the dns of compressible turbulence. *Physics of Fluids*, 9(1):4–6.
- [69] Roache, P. J. (2001). Code Verification by the Method of Manufactured Solutions . *Journal of Fluids Engineering*, 124(1):4–10.
- [70] Roy, C. J. (2005). Review of code and solution verification procedures for computational simulation. *Journal of Computational Physics*, 205(1):131–156.
- [71] Sagaut, P. and Cambon, C. (2008). *Homogeneous turbulence dynamics*, volume 10. Springer.
- [72] Samtaney, R., Pullin, D. I., and Kosović, B. (2001). Direct numerical simulation of decaying compressible turbulence and shocklet statistics. *Physics of Fluids*, 13(5):1415–1430.
- [73] Sandham, N. D., Li, Q., and Yee, H. C. (2002). Entropy splitting for high-order numerical simulation of compressible turbulence. *Journal of Computational Physics*, 178(2):307–322.
- [74] Shu, C.-W. (1998). Essentially non-oscillatory and weighted essentially non-oscillatory schemes for hyperbolic conservation laws. In *Advanced Numerical Approximation of Nonlinear Hyperbolic Equations*, pages 325–432. Springer.
- [75] Sjörn, B. and Yee, H. C. (2018). High order entropy conservative central schemes for wide ranges of compressible gas dynamics and MHD flows. *Journal of Computational Physics*, 364:153–185.
- [76] Slotnick, J., Khodadoust, A., Alonso, J., Darmofal, D., Gropp, W., Lurie, E., and Mavriplis, D. (2014). Cfd vision 2030 study: A path to revolutionary computational aerospace. *NASA-CR-2014-218178*.
- [77] Söderlind, G. (2003). Digital filters in adaptive time-stepping. *ACM Transactions on Mathematical Software*, 29(1):1–26.
- [78] Söderlind, G. and Wang, L. (2006). Adaptive time-stepping and computational stability. *Journal of*

Computational and Applied Mathematics, 185(2):225–243.

- [79] Svärd, M., Carpenter, M. H., and Parsani, M. (2018). Entropy stability and the no-slip wall boundary condition. *SIAM Journal on Numerical Analysis*, 56(1):256–273.
- [80] Svärd, M. and Nordström, J. (2014). Review of summation-by-parts schemes for initial-boundary-value-problems. *Journal of Computational Physics*, 268(1):17–38.
- [81] Svärd, M. and Özcan, H. (2014). Entropy-stable schemes for the Euler equations with far-field and wall boundary conditions. *Journal of Scientific Computing*, 58(1):61–89.
- [82] Tadmor, E. (2003). Entropy stability theory for difference approximations of nonlinear conservation laws and related time-dependent problems. *Acta Numerica*, 12:451–512.
- [83] Wang, Z., Fidkowski, K., Abgrall, R., Bassi, F., Caraeni, D., Cary, A., Deconinck, H., Hartmann, R., Hillewaert, K., Huynh, H., Kroll, N., May, G., Persson, P.-O., Leer, B., and Visbal, M. (2013). High-order cfd methods: current status and perspective. *International Journal for Numerical Methods in Fluids*, 72(8):811–845.
- [84] Winters, A. R., Derigs, D., Gassner, G. J., and Walch, S. (2017). Uniquely defined entropy stable matrix dissipation operator for high Mach number ideal MHD and compressible Euler simulations. *Journal of Computational Physics*, 332(1):274–289.
- [85] Winters, A. R. and Gassner, G. J. (2015). A comparison of two entropy stable discontinuous Galerkin spectral element approximations to the shallow water equations with non-constant topography. *Journal of Computational Physics*, 301(1):357–376.
- [86] Winters, A. R., Moura, R. C., Mengaldo, G., Gassner, G. J., Walch, S., Peiro, J., and Sherwin, S. J. (2018). A comparative study on polynomial dealiasing and split form discontinuous Galerkin schemes for under-resolved turbulence computations. *Journal of Computational Physics*, 372:1 – 21.
- [87] Yamaleev, N. K. and Carpenter, M. H. (2017). A family of fourth-order entropy stable non-oscillatory spectral collocation schemes for the 1-d Navier-Stokes equations. *Journal of Computational Physics*, 331:90–107.
- [88] Yee, H. C., Vinokur, M., and Djomehri, M. J. (2000). Entropy splitting and numerical dissipation. *Journal of Computational Physics*, 162(1):33–81.
- [89] Zhu, J., Zhong, X., Shu, C.-W., and Qiu, J. (2013). Runge–Kutta discontinuous Galerkin method using a new type of WENO limiters on unstructured meshes. *Journal of Computational Physics*, 248:200 – 220.